Transient lagging chromosomes cause primary microcephaly

*Elena Doria[1,2], *Daria Ivanova[1,2], Alexandre Thomas[1,2] and Patrick Meraldi[1,2]

[1]Department of Cell Physiology and Metabolism, Faculty of Medicine, University of Geneva, 1211 Geneva 4, Switzerland

[2]Translational Research Centre in Onco-hematology, Faculty of Medicine, University of Geneva, 1211 Geneva 4, Switzerland

* Equal contribution

Correspondence to: patrick.meraldi@unige.ch - ORCID: 0000-0001-9742-8756

ABSTRACT

Primary microcephaly is caused by the depletion of neuronal progenitor cells during brain development, resulting in reduced brain size and impaired cognitive abilities. It arises due to recessive loss-of-function mutations of cell division genes, that are thought to cause neuronal progenitor loss either because of aneuploidy-driven apoptosis, spindle orientation defects, or prolonged mitotic timing. Loss of the two most frequently impaired microcephaly genes, *WDR62* and *ASPM*, elicits, however, none of these phenotypes in human cells. Instead, their loss slows down poleward microtubule flux and results in transient lagging chromosomes in anaphase. Whether these defects cause primary microcephaly is, however, unknown. Here we show that slower poleward microtubule flux rates lead to transient lagging anaphase chromosomes that elicit an Aurora-B dependent activation of 53BP1 and the p53-target p21, impairing cell proliferation. Co-depletion of CAMSAP1, an inhibitor of microtubule depolymerization at spindle poles, restores normal poleward flux rates, suppresses the lagging chromosomes, silences 53BP1 and p21 activation, and allows normal cell proliferation in WDR62-depleted cells. In *Drosophila melanogaster* larvae knock-down of the CAMSAP1 ortholog Patronin suppresses the small brain, the neuroblast depletion, and the impaired cognitive phenotype associated with WDR62 loss. We thus postulate that poleward microtubule flux defects in neuronal progenitor cells drive primary microcephaly due to the activation of 53BP1 and p21 in response to transient lagging chromosomes in anaphase. Since loss of most cell division genes associated with primary microcephaly can lead to such transient lagging chromosomes, we speculate that they might represent a common cause of this disease.

INTRODUCTION

Autosomal recessive primary microcephaly (microcephaly primary hereditary [MCPH]) leads to smaller brain size in new-borns due to exhaustion of neuronal progenitor cells (*1*). Recessive loss-of-function mutations in 30 different genes, most of which involved in cell cycle and cell division, are linked to this disease. This includes genes encoding key regulators of centriole biogenesis (*PLK4, SAS6, STIL, SAS4, CEP152* and *CEP135),* pericentriolar proteins (*CDK5RAP2, PCNT, TUBGCP4* and TUBGCP6*),* microtubule-associated proteins and microtubule-motors of the mitotic spindle (*ASPM, WDR62, MAP11*, *KIF11* and *KIF14*), kinetochore proteins (*KNL1* and *CENP-E),* and regulators of DNA damage/condensation/replication (*MCPH1, ORC1, ORC4, ORC6, CDC45, NCAPH, NCAPD2* and *NCAPD3)* (*2–5*). The common denominator between those genes remains unknown. For the cell division genes, several non-exclusive hypotheses have been postulated: (1) chromosome segregation errors that lead to aneuploidy and result in neuronal progenitor pool depletion via p53-induced apoptosis (*6*); (2) erroneous spindle orientation that drives premature neuronal differentiation depleting the neuronal progenitor pool (*7–9*), (3) or centrosomal defects that prolong mitosis, causing an activation 53BP1 that triggers a p53-dependent cell proliferation defect (*10*). However, loss of function of WD Repeat-Containing Protein 62 (*WDR62*, MCPH2) and the abnormal spindle-like microcephaly associated gene (*ASPM*, MCPH5), which account for over 80% of all microcephaly cases (*11*), has not been conclusively linked to aneuploidy, spindle mis-orientation or a mitotic delay in human cells (*12–14*).

Instead, WDR62 and ASPM regulate microtubule dynamics by recruiting the microtubule-severing enzyme Katanin to mitotic spindle poles (*14–16*). Impairment of either protein results in insufficient microtubule minus-end depolymerization and reduced poleward microtubule flux rates (*14–16*), a conveyor belt-like movement that drives tubulin subunits towards the minus ends at spindle poles (*17*). We previously showed that human WDR62 depletion does not delay mitosis, but instead leads in anaphase to transient lagging chromosomes that are nevertheless incorporated into the daughter nuclei (*14*). Whether these transient chromosome segregation defects are linked to microcephaly remains unknown.

Here, we show that transient lagging chromosomes in anaphase in WDR62- or ASPM-depleted human cells elicit an Aurora-B dependent response that activates 53BP1 in the ensuing G1 phase, impairing cell proliferation. We hypothesized that such mild segregation defects, which are frequently seen after the loss of most MCPH genes, could be a common origin for the reduced proliferation of neuronal progenitor cells. To test this hypothesis, we co-depleted CAMSAP1, a member of the Patronin/CAMSAP family, which inhibits spindle-associated microtubule depolymerases of the kinesin-13 family at spindle poles (*18–22*). CAMSAP1 co-depletion in WDR62 RNAi background restored normal poleward flux rates, suppressed the appearance of transient lagging chromosomes and 53BP1 activation, and rescued cell proliferation in human cells and microcephaly in *Drosophila melanogaster* larvae. We postulate that transient lagging chromosomes in anaphase are a major cause of primary microcephaly.

RESULTS

Depletion or deletion of WDR62 in human tissue culture cells leads to decreased microtubule depolymerization at spindle poles, slower poleward microtubule flux rates, and transient lagging chromosomes in anaphase (*14*). Such chromosomes (also called lazy chromosomes) transiently lag behind the DNA masses during anaphase in WDR62-depleted cells but, unlike persistent lagging chromosomes, are incorporated into the daughter nuclei without the formation of micronuclei (*14*, *23*). Such transient lagging anaphase chromosomes were visible in live WDR62-depleted cells stained with SiR-DNA (a cell was considered to have a transient lagging chromosome if a chromosome arm was sticking out of the DNA mass by more than 2 μm as the two DNA masses were separated by a minimum of 6 μm; $p = 0.0368$ in Chi-square test; Figure 1A and B and Supplementary Figure 1A and B for siRNA validation), but also in WDR62-depleted RPE1 cells expressing the kinetochore marker GFP-CENP-A and the centrosome marker GFP-Centrin1, indicating that they reflect asynchronous kinetochore movements (Supplementary Figure 1C and D). Transient lagging chromosomes have so far not thought to lead to DNA damage. Nevertheless, since primary microcephaly has been genetically also linked to DNA damage signalling, we tested whether WDR62 depletion activated such pathways. We stained

non-transformed retina pigment epithelial cells expressing human telomerase (hTert-RPE1) for γH2AX and 53BP1 after control or WDR62 depletion, or after treatment with the DNA-damaging agent Doxorubicin. Both form nuclear foci upon activation: while γH2AX labels double-strand breaks (*24*), 53BP1 is involved in double-strand break repair, but also in p53 stabilization after long mitotic delays (*25–29*). This drives the expression of the cyclin-dependent kinase inhibitor p21, a key p53 target, resulting in cell cycle delay or arrest (*30*). Using automatic image analyses (Supplementary Figure 1E), we analysed hundreds of interphase cells per experiment for the presence of γH2AX or 53BP1-positive nuclei. In each independent experiment, WDR62 depletion increased the proportion of cells with 53BP1-positive nuclei, leading on average to an increase from 31% (siControl) to 42% (siWDR62; overall $p < 0.0001$ in Fischer's exact test, Fig. 1C and D). In contrast, WDR62 depletion did not increase the proportion of γH2AX-positive cells (Supplementary Figure 1F and G). WDR62-depleted cells typically displayed single nuclear 53BP1-positive foci, while doxorubicin-treated cells (condition representing DNA damage) displayed dozens of 53BP1 foci (Figure 1C). Quantitative immunofluorescence measurements on the same cells indicated that WDR62-depleted cells also had elevated nuclear p21 levels ($p < 0.0001$ in Fisher's exact test; Figure 1C and E), implying a cell cycle delay. Consistently, when we labelled control- or WDR62-depleted cells with cell proliferation pulse-chase marker CFSE (Carboxyfluorescein succinimidyl ester, Supplementary Figure 1H for methodology), and let them proliferate for 5 days, we found that control-depleted cells underwent two full divisions more than serum-starved cells, whilst WDR62-depleted cells only underwent 1.5 cell divisions more ($p = 0.0029$ in one way ANOVA; Figure 1F and G). This implied WDR62-depletion activates the 53BP1-p53-p21 signalling pathway and delays cell proliferation independently of double-strand breaks.

Transient lagging chromosome induce 53BP1 foci via Aurora B signalling.

53BP1 is activated in the absence of DNA damage, but also if cells are delayed in mitosis, for example after centrosome loss (*27–29*). Aneuploidy can also activate p53 (*31*). WDR62 depletion, however, does not lead to a mitotic delay or micronuclei, nor does it affect centrosome numbers (*14*). Moreover, metaphase spreads indicated that WDR62-depleted cells were euploid; in contrast cells treated with

Reversine, a known inducer of aneuploidy that inhibits the spindle assembly checkpoint kinase Mps1, displayed severe aneuploidy ((*32*); Figure 2A and B). We next reasoned that 53BP1 activation could be linked to the transient lagging chromosomes, or alternatively be linked to an unrelated cell-cycle function of WDR62. To distinguish between the two possibilities, we tested whether the 53BP1-positive foci temporally correlated with the presence of transient lagging chromosomes. When we monitored WDR62-depleted 53BP1-GFP RPE1 live cells in the presence of the chromosome marker SiR-DNA (*33*), we found that 53BP1 nuclear foci were 18 times more likely to appear in the next interphase in cells having experienced a transient lagging chromosome ($p < 0.0001$ in Fischer's exact test; Figure 2C and D). This suggested that transient lagging chromosomes were the upstream cause for 53BP1 activation. Consistently, depletion of ASPM also led to the appearance of transient lagging chromosomes and 53BP1 foci (Figure 2E-G-F, and supplementary Figure 2A and B for siRNA validation).

Why would transient lagging chromosomes in anaphase activate 53BP1? One possibility is that transient lagging chromosomes are exposed longer to the activity gradient of the mitotic kinase Aurora B at the spindle mid-zone, an activity known to delay nuclear envelope reformation (*34*, *35*), which has been proposed to activate p53 in the presence of permanent lagging chromosomes (*36*, *37*). We reasoned that if this was true, maintaining Aurora B on anaphase chromosomes should lead to more 53BP1-positive cells. Indeed, Aurora B is extracted from chromosomes at anaphase onset via Cdc48/p97 and the de-ubiquitinase UBASH3B, allowing its transport to the spindle midzone (*35*, *38*, *39*). Partial depletion of the Cdc48/p97 co-factor NPL4, or of UBASH3B, delayed chromosomal Aurora-B extraction in anaphase and led, as predicted, to more 53BP1-positive cells (Figure 2H - M), despite the absence of a mitotic delay or lagging chromosomes (Supplementary Figure 2 G-I). Conversely, partial inhibition of Aurora B with 50 nM Barasertib, a condition that reduced the localization of the Aurora B substrate MCAK at kinetochores by 60% ((*40*) Supplementary Figure 2J, K), abolished the increase in 53BP1-positive nuclei in WDR62-depleted cells (Fig. 2M and N). We thus hypothesized that a deregulation of poleward microtubule flux in WDR62-depleted cells favours the appearance of transient

lagging chromosomes in anaphase that activate 53BP1 via Aurora B in the next G1 phase, delaying cell cycle progression.

Co-depletion of CAMSAP1 rescues poleward microtubule flux rates and lagging chromosomes in WDR62-depleted cells.

To test this hypothesis, we aimed to restore normal poleward microtubule flux rates in WDR62-depleted cells. One promising candidate was the depletion of CAMSAP1, a member of the CAMSAP protein family, which we found to localize to spindle poles in mitotic cells (Figure 3A and B). CAMSAP1-3 proteins and their *Drosophila melanogaster* ortholog Patronin inhibit the microtubule depolymerizing activity of kinesin-13s; moreover, *PATRONIN* mutations increase poleward microtubule flux rates in flies (*18–20*). In RPE1 cells, CAMSAP1 depletion increased poleward microtubule flux rates in metaphase by 50% and doubled the percentage of cells displaying transient lagging chromosomes (Figure 3C-F). This suggested that both a reduction and an increase in poleward microtubule flux can impair efficient anaphase chromosome movements. Co-depletion of CAMSAP1 and WDR62, in contrast, restored normal poleward microtubule flux rates (Figure 3G-K) and rescued the transient lagging chromosome phenotype (Figure 3L). We conclude that the reduction of poleward microtubule flux causes lagging chromosomes in WDR62-depleted cells, and that efficient anaphase chromosome movements require a balanced microtubule flux rate.

Co-depletion of CAMSAP1 in WDR62-depleted cells suppresses activation of the 53BP1 and p21 and restores normal cell proliferation.

We next found by quantitative immunofluorescence that CAMSAP1 co-depletion also suppressed the appearance of 53BP1 foci and the accumulation of nuclear p21 in WDR62-depleted cells (Figure 4A-C). Moreover, co-depletion of CAMSAP1 in a WDR62 siRNA background also restored normal cell proliferation, as quantified with the 5-day CFSE assay (Figure 4D). This confirmed our hypothesis that reduced poleward microtubule flux rates and transient lagging chromosomes activate 53BP1 and drive p21 expression to induce a cell proliferation delay.

Nevertheless, we also noted that cells depleted of CAMSAP1 alone, neither accumulated p21 (Figure 4D) nor experienced a cell proliferation defect (Figure 4A), despite transient lagging chromosomes (Figure 3F) and an increased proportion of cells with 53BP1-foci (Figure 4B and C). How was this possible? A detailed live-cell investigation of the life-time of transient lagging chromosomes in anaphase and the timing of appearance of 53BP1 foci revealed key differences: (1) while transient lagging chromosomes in WDR62-depleted cells persisted in anaphase for a median time of 3.5 mins, the corresponding median time in CAMSAP1-depleted cells was only 2 mins ($p < 0.0001$ in Mantel-Cox test); (2) the 53BP1 foci appeared on average 1 hour after anaphase in WDR62-depleted cells, but only after 2 hours in CAMSAP1-depleted cells ($p = 0.0038$ in unpaired t-test, Figure 4E and F). This suggested that the response to transient lagging chromosomes is gradual and that cells will only induce p21 expression if chromosomes are present in the spindle midzone for 3-4 mins or longer, and that laggards that remain there for shorter times will not fully activate 53BP1 and p21. These findings are also consistent with the fact that unperturbed cells often experience transient lagging chromosomes for brief periods without impairing cell proliferation. Indeed, the lifetime of the few lagging chromosomes in control-depleted or WDR62/CAMSAP1-depeleted cells was as short as in CAMSAP1-depleted cells (Figure 4E). We conclude that poleward microtubule flux defects lead to transient lagging chromosomes that, if not rapidly resolved, will activate 53BP1 and p21 to delay cell proliferation.

Patronin co-depletion restores brain size and cognitive function in WDR62-depleted fly larvae

Given that primary microcephaly is caused by an exhaustion of neuronal progenitor cells, and that an extension of the cell cycle timing in murine progenitors causes a premature cell differentiation (*41*), we hypothesized that the proliferation impairment we observed could explain the origin of microcephaly in organisms lacking WDR62. To test this hypothesis, we turned to *Drosophila melanogaster* larvae, where *WDR62* mutations cause a cell cycle delay and a brain size reduction (*42*). We used the UAS/Gal4 system (*43*) to express UAS-*WDR62* and UAS-*Patronin* RNAi constructs (*WDR62* RNAi and *Patronin* RNAi hereafter, Supplementary Figure 3B) specifically in the brain and efficiently decrease their respective mRNA and protein levels (*44*, *45*). We first tested whether Patronin co-depletion counteracts the effects of WDR62 RNAi on brain lobe size. To compare brain size of larvae of similar age, egg-

laying was staged and the resulting third instar larvae were stained with the DNA-marker DAPI and the neuroblast-specific polarity marker Miranda ((*46*); Figure 5A and B). Consistent with previous studies, brain size ($p = 0.0038$ in mixed-effect analysis) and neuroblast numbers in the central brain ($p = 0.0041$ in one-way Anova) was decreased by roughly one quarter in *WDR62* RNAi compared to control conditions (Figure 5A-D). Patronin RNAi had no effect on its own but led to larger brain lobes and restored neuroblast numbers in a *WDR62* RNAi background (Figure 5A-D), indicating a rescue of the microcephaly phenotype. Miranda staining also allowed us to probe the polarity of the neuroblasts and spindle orientation vs the polarity axis ((*46*); Figure 5E). We observed the typical Miranda crescents in all conditions and found no change in spindle orientation (Figure 5F), indicating that the brain size phenotypes occurred independently of cell polarity or spindle orientation.

To test whether the reduction in brain size in WDR62-depleted cells impairs larval cognitive functions, we performed two basic behavioural assays. In the first assay we recorded larvae on agar plates as they searched for food (Figure 5G and supplementary figure 3C). Wild-type larvae optimize their search strategy by turning by 90° after 3-4 contractions (*47*). In contrast, *WDR62* RNAi-treated larvae turned much less frequently, leading them to unidirectional movements (11 median contraction per turn, $p < 0.0001$; Figure 5H and supplementary Figure 3C). This defect was rescued by *Patronin* co-depletion (3 median contractions per turn; Figure 5H and supplementary Figure 3C). Second, we plated larvae on agar plates containing in one half fructose and in the other half no fructose and recorded the position of the larvae after 5 minutes. As previously described, wild-type larvae selectively chose the fructose containing half-plate (76%; (*48*)); in contrast, WDR62 RNAi larvae showed a much weaker preference for fructose (57% $p = 0.0319$ in Fischer's exact test; Figure 5I and J, supplementary Figure 3D). This cognitive defect was again rescued by *Patronin* co-depletion (77%, Figure 5J). We concluded that co-depletion of Patronin rescues the microcephaly phenotype induced by WDR62 depletion in terms of brain size, neuroblast depletion and basic cognitive functions.

DISCUSSION

Loss of function of WDR62 or ASPM causes over 80% of the primary microcephaly cases (*11*). These cases, however, are not due to the postulated cellular origins for primary microcephaly: excessive

mitotic duration, loss or gain of chromosomes, or spindle orientation defects (*6*, *8–10*, *49*). Instead, our *in vitro* and *in vivo* results indicate that a deregulation of microtubule minus-end dynamics, which leads to transient lagging chromosomes that elicit an Aurora-B dependent activation of 53PB1 and the p53-target p21, impairs cell cycle progression thus limiting the number of neuronal progenitor cells (see model Figure 5K). We postulate that this response is due to a surveillance mechanism that reacts to chromosomes that are not segregated in time with the rest of the chromosome mass in anaphase, complementing the mitotic surveillance mechanism that checks whether cells have remained for too long in mitosis (*26–29*, *50*). Given that loss of many cell division genes associated to primary microcephaly leads to transient lagging chromosomes, we speculate that this mechanism could be a frequent cause of this disease.

One major difficulty when evaluating the potential cellular causes of primary microcephaly, has been the lack of effective rescue experiments that could validate the hypotheses. Indeed, it is difficult to correct for aneuploidy, spindle orientation defects or excessive mitotic timing without introducing additional mitotic defects that may have confounding effects. Here however, by combining WDR62 and CAMSAP1 depletion and restoring normal minus-end microtubule dynamics, we could rescue all the downstream effects of WDR62 depletion at the cellular level, establishing a causal chain of events. The fact that this co-depletion restored neuroblast numbers and basic cognitive function in WDR62-depleted fly larvae, backs the hypothesis that defects in microtubule minus-end dynamics cause primary microcephaly in WDR62-depleted flies. Our data also imply that the speed of poleward microtubule flux needs to be balanced, as both an increase and a decrease in speed will lead to asynchronous anaphases. Nevertheless, we also note that the rescue after WDR62/CAMSAP1 co-depletion is not perfect: co-depletion of *WDR62* and *Patronin* results in larvae with larger brain size but normal numbers of neuroblast. Whether that increase in size is due to an increase in cell size or an excess in proliferation is not clear. These cells, however, did not resemble tumour cells, as their cell polarity was preserved.

Work in the last 15 years have shown that cells not only possess a spindle checkpoint that monitors kinetochore-microtubule attachment in metaphase (for review see (*51*)), but also a mitotic duration surveillance mechanism, which induces a 53BP1/USP28-dependent activation of p53 to block the cell

cycle when cells have spent more than 90 minutes in mitosis (*26–29*, *50*). This ensures that cells that have encountered difficulties in satisfying the spindle assembly checkpoint are impaired in their proliferation. Here, we propose the existence of another, complementary surveillance mechanism that monitors chromosome movements in anaphase and activates 53BP1 in the presence of transient lagging chromosomes. This mechanism is distinct from the mitotic timing surveillance system, as WDR62-depleted cells have a normal mitotic timing. It may allow cells to react to erroneous kinetochore-microtubule attachments that cannot be detected by the spindle assembly checkpoint and do not extend mitotic timing, such as merotelic kinetochore-microtubule attachments (one kinetochore bound by microtubules from both spindle poles; (*52*)). Such merotelic attachments are often transiently lagging in anaphase and rapidly corrected by Aurora B (*23*, *53*, *54*); such a surveillance system would allow to detect those transient lagging chromosomes that are not immediately corrected and potentially prevent the proliferation of cells having experienced such a segregation error. Indeed, lagging chromosomes can contribute to chromosome compaction and nuclear architecture defects in the absence of aneuploidy and impair post-natal growth in mice (*55*). This surveillance mechanism detects the proximity of anaphase chromatin to Aurora-B activity and not the lagging per se, as it can be activated in Npl4- or UBASH3B-depleted cells without lagging chromosomes or mitotic delay. Whether this is due to the ability of Aurora-B to delay nuclear envelope reformation on lagging chromosomes (*34*, *35*), remains to be seen. Our hypothesis also reflects the gradual response we observe for this surveillance mechanism (Figure 5K): lagging chromosomes in CAMSAP1-depleted cells persist only 1-2 minute and lead to a weak response that does not impair cell proliferation; in contrast transient lagging chromosomes that persist for 3-4 minutes, as seen in WDR62 depleted cells, are associated with a rapid 53BP1 foci formation and p21 activation. Such a semi-permissive mechanism also fits with the observation that short-lived transient lagging chromosomes can be observed in 20-30% of wild-type RPE1 cells. Nevertheless, partial Aurora-B inhibition significantly reduced the percentage of 53BP1-positive cells in wild-type condition (Figure 2N), suggesting that this surveillance mechanism might constantly impair the proliferation of a subset of cells.

Finally, we speculate that primary microcephaly might be caused by the frequent incapacity to satisfy this surveillance mechanism in time, due to transient lagging chromosomes. This disease is caused by the loss of over 30 different genes, many of which are linked to cell division and chromosome segregation. Although it is likely that several cellular mechanisms can contribute to neuronal progenitor exhaustion, we note that transient lagging chromosome are likely to appear in most of those genetic backgrounds, such as defective centriole biogenesis, impaired centrosome function, or loss of microtubule associated proteins, microtubule motors or kinetochore proteins, and might thus represent a common cellular origin. These mild defects would be sufficient to affect the expansion of neuronal progenitor cells, which have very short cell cycle, without impairing the overall development of the other organs. The mildness of these defects may also explain why patients having lost WDR62 or APSM do not display an elevated risk for cancer development, unlike patients with a predisposition to aneuploidy (*56*).

ACKNOWLEDGEMENTS

We thank A. Khodjakov (State University of New York), R. Medema (Netherland Cancer Institute), E.Nagoshi (University of Geneva) and R.Giet (University of Rennes) for reagents, the HumanaFly facility and M. Savitskiy (University of Geneva) for drosophila support, the Bioimaging Facility and N. Liaudet (University of Geneva) for microscopy support; the Flow Cytometry Core Facility (University of Geneva) for FACS support; S. Barbieri (University of Geneva) for help with data analysis, H. Maiato (University of Porto), Iva Tolic (Ruđer Bošković Institute), M. Gotta and her laboratory (University of Geneva), and members of the Meraldi laboratory for critical discussions. This work in the Meraldi laboratory is supported by the Swiss National Science Foundation project grants (208052 & 215124) and the University of Geneva.

Competing interests

The authors declare no competing interests.

Author contributions:

The project was initiated by E.D., D.I. and P.M. and directed by P.M.; E.D. and D.I. performed all experiments; A.T. contributed to the drosophila experiments; E.D., D.I. and P.M. analyzed and interpreted all the results; E.D., D.I., A.T. and P. M. wrote the manuscript.

FIGURE LEGENDS

Figure 1: WDR62 depletion leads to 53BP1 and p21 activation and a proliferation delay. (**A**) Time-lapse single-plane images RPE1 cells stained with SiR-Tubulin (red) and SpY-DNA (white) showing examples of transient or persistent lagging chromosomes (green arrows). Scale bars = 5 µm. (**B**) Quantification of transient lagging chromosomes in *siWDR62*-treated RPE1; n = 46-57 cells, * p= 0.0368 in Chi-square test. (**C**) Immunofluorescence images of interphase RPE1 cells treated with *siCTRL*, *siWDR62* or Doxorubicin, and stained with DAPI, 53BP1 and p21 antibodies. Blue dotted lines represent 53BP1-negative nuclei, red dotted lines represent 53BP1-positive nuclei. Scale bars = 10 µm. (**D**) Quantification of 53BP1 positive cells. Connected dots represent paired experiment. N = 4 independent experiments, n = 648 – 1440 cells; ****, p < 0.0001 in Fisher's exact test (**E**) Quantification of p21 positive cells. Connected dots represent paired experiment. Blue dotted lines represent p21-negative nuclei, red dotted lines represent p21-positive nuclei. N = 6, n = 570-1010 cells; ****, p < 0.0001 in Fisher's exact test; (**F**) Example of FACS CFSE analysis data (**G**) Quantification of cell divisions after 5 days beyond serum starvation based on CFSE intensity, N = 4, *n* = 18194 - 82963 cells; **, p = 0.0029, in one-way ANOVA. Error bars represent SEM.

Figure 2: Transient lagging chromosomes activate 53BP1 via Aurora B (A) Chromosomes spread of RPE-1 cells stained with DAPI. Scale bar = 10 µm **(B)** Quantification of chromosomes number of RPE-1 cells treated with *siCTRL*, *siWDR62* or Reversine. N = 35-40 cells; *siCTRL* vs Reversine p < 0.0001, in two-way Anova **(C)** Time lapse imag of RPE-1 53BP1-GFP cell treated with *siWDR62* in G2 (top row, blue dotted circle 53BP1-negative), anaphase (middle row) and in the ensuing G1 phase (bottom row, red dotted circlle 53BP1-positive). White arrow indicates transient lagging chromosome. Scale bars = 10 µm **(D)** Quantification of *siWDR62*-treated 53BP1-GTP positive cells after a cell

division with or without lagging chromosomes. $p < 0.0001$, Fisher's exact test. **(E)** Quantification of lagging chromosome in SiR-DNA stained live RPE-1 cells treated with *siCTRL* or *siASPM*. n = 34-92 cells; p = 0.0031, Fisher's exact test. **(F)** Immunofluorescence images of siCTRL- or siASPM-treated RPE-1 cells stained for 53BP1 and DAPI. Blue dotted circles represent 53BP1- nuclei, red ones 53BP1 positive nuclei. **(G)** Quantification of 53BP1 positive cells after *siCTRL* (n=1556 cells), *siASPM* (n=1224 cells) or Doxorubicine (n=681 cells) treatment. N = 6, n = 681-1556 cells; connected dots represent paired experiment. **** $P < 0.0001$, Fisher's exact test. **(H)** Immunofluorescence of RPE-1 cells after *siCTRL*, *siNPL4* or *siUBASH3B* treatment stained for AuroraB and DAPI. Scale bars = 5 µm **(I and J)** AuroraB intensity quantification in anaphase RPE-1 cells treated with *siCTRL*, *siNPL4* or *siUBASH3B*. Y-axes indicate Aurora B intensity on DNA normalized to background; x-axes indicates the distance between the two DNA masses reflecting anaphase progression, dotted lines represent 95% confidence intervalls, n = 77 -113 cells. **(K and L)** Quantification of 53BP1 positive cells after *siCTRL*, *siNPL4* (K) or *siUBASH3B* (L) treatment. N=5, n = 1191-2062 cells, connected dots represent paired experiment. $P < 0.0001$, Fisher's exact test. **(M)** Immunofluorescence images of RPE-1 cells treated with indicated treatments and stained for 53BP1 and DAPI. Light blue dotted circles represent 53BP1- nuclei, red ones 53BP1 positive nuclei. Scale bars = 10 µm **(N)** Quantification of 53BP1 positive cells after *siCTRL*, *siCTRL* + barasertib, *siWDR2*, *siWDR62* + barasertib) treatments. N=3, n = 588-771 cells; connected dots represent paired experiments. **** $P < 0.0001$, Fisher's exact test.

Figure 3: CAMSAP1 co-depletion rescues the transient lagging chromosomes in WDR62-depleted cells (A) Immunofluorescence of RPE-1 cells treated with *siCTRL* or *siCAMSAP1* stained for CAMSAP1 and DAPI. **(B)** Quantification of normalized CAMSAP1 level in RPE-1 cells treated with *siCTRL* (n=55 cells) and *siCAMSAP1* (n=47 cells). N = 3, n = 47-55 cells, **** $p < 0.0001$, student t-test. **(C)** Scheme of photoactivation assay for microtubules poleward flux measurement. **(D)** Quantification of microtubule poleward flux speed in RPE-1 PAGFP-αtubulin cells treated with *siCTRL* and *siCAMSAP1*. N= 3, n = 33-39 cells, **** $p < 0.0001$, student t-test. **(E)** Stills of RPE-1 GFP-Centrin1/GFP-CENPA cells in a normal anaphase or an anaphase with a transient lagging kinetochore. **(F)** Quantification of transient lagging chromosomes in 15 minutes live cell movies of

RPE1 GFP-Centrin1/GFP-CENPA cells treated with *siCTRL* or *siCAMSAP1*, n = 66-71 cells, *** p = 0.0009, Fisher's exact test. **(G)** Immunofluorescence images of RPE-1 cells treated with *siCTRL*, *siCAMSAP1*, *siWDR62*, or *siCAMSAP1 + siWDR62,* stained for CAMSAP1 (left panels), WDR62 (right panels) and DAPI. **(H and I)** Quantification of normalized CAMSAP1 (H) and WDR62 (I) level in RPE-1 cells treated with indicated siRNAs. N=3, n = 66-95 cells, **** $p < 0.0001$; One-way Anova test. **(J)** Live cell images RPE-1 PAGFP-αtubulin cells treated with *siCTRL*, *siCAMSAP1*, *siWDR62, siCAMSAP1+siWDR62* before and after photoactivation **(K)** Quantification of microtubule poleward flux speeds in RPE-1 PAGFP-αtubulin cells treated with *siCTRL*, siCAMSAP1, siWDR62, siCAMSAP1+siWDR62. N = 3, n = 28-47 cells, **** $p < 0.0001$; One-way Anova test. **(L)** Percentage of RPE-1 GFP-Centrin1/GFP-CENPA cells with transient lagging chromosomes after indicated siRNA treatments. Lagging chromosomes were quantified as shown in (E); n = 29-48 cells; *siCTRL vs siCAMSAP1* p = 0.0040, *siCTRL vs siWDR62* p = 0.0317, *siWDR62 vs siCAMSAP1+siWDR62* p = 0.0098; Fisher's exact test. All scale bars = 5 µm.

Figure 4: Camsap1 co-depletion rescues WDR62 RNAi phenotype. (**A**) Immunofluorescence images of interphase RPE1 cells treated with *siCTRL*, *siCAMSAP1*, *siWDR62*, *siCAMSAP1+siWDR62* and Doxorubicin, stained with DAPI, 53BP1 and p21 antibodies. Blue dotted circles represent 53BP1-negative nuclei, red ones 53BP1-positive nuclei. Scale bars = 10 µm. (**B**) Quantification of 53BP1 positive cells after indicated siRNA treatments. Connected dots represent paired experiment. N = 4, n = 648 – 1440 cells; *siCTRL vs. siWDR62*, ***, p = 0.0002; *siCTRL vs. siCAMSAP1*, *, p = 0.0127; *siWDR62 vs. siCAMSAP1 + siWDR62,* *** p = 0.0006; Fisher's exact test. (**C**) Quantification of p21 positive cells in indicated siRNA treatments. Connected dots represent paired experiment. Blue dotted circles represent p21-negative nuclei, red one p21-positive nuclei. N = 5, n = 1020 – 1330 cells; ****, $p < 0.0001$; Fisher's exact test. (**D**) Quantification of cell divisions above serum starvation in CFSE assay in indicated siRNAs, N = 4, n = 18194-82963 cells; *, *siCTRL vs. siWDR62,* p = 0.0224: *siWDR62 vs. siCAMSAP1 + WDR62*, p = 0.0319 RM (repeated measurements) mixed effect analysis; error bars represent SEM. (**E**) Quantification of persistence of transient lagging chromosomes in *siCAMSAP1* and siWDR62-treated RPE1 GFP-CenpA/GFP-Centrin1 cells recorded by fluorescent time

lapse microscopy, N = 4, n =43 - 59 cells; ** p = 0.0011, Wilcoxon test. (**F**) Time of 53BP1 appearance in *siCAMSAP1* and *siWDR62*-treated RPE1 GRP-53BP1 live cells having experienced a lagging chromosome, N = 8, n =15-19 cells; **, p = 0.0062, Mann-Whitney test.

Figure 5: Co-depletion of Patronin rescues small brain phenotype in WDR62 RNAi background

(A) Brains extracted from *D. melanogaster* larvae of w^{1118}, *PatroninRNAi*, *WDR62RNAi*, and *PatroninRNAi + WDR62RNAi*, stained with DAPI. The dotted red circle represents the area of the right lobe from w^{1118} brain superposed on *PatroninRNAi*, *WDR62RNAi*, *PatroninRNAi+ WDR62RNAi* brains. **(B)** Brain lobes area quantification of *D. melanogaster* larvae brains extracted from w^{1118} (n= 73 lobes), *PatroninRNAi* (n= 56), *WDR62RNAi* (n= 76), *PatroninRNAi+ WDR6RNAi* (n= 23) larvae., w^{1118} vs *WDR62RNAi* $p < 0.0001$, w^{1118} vs *PatroninRNAi + WDR62RNAi* $p < 0.0001$, *WDR62RNAi* vs *PatroninRNAi + WDR62RNAi* $p < 0.0001$, one-way Anova test. **(C)** Quantification of neuroblast stained with Miranda antibodies in brains extracted from w^{1118} (n= 9 brains), *PatroninRNAi* (n= 8), *WDR62RNAi* (n= 15), *PatroninRNAi+ WDR6RNAi* (n= 10) larvae, w^{1118} vs *WDR62RNAi* p = 0.0041, *WDR62RNAi* vs *PatroninRNAi + WDR62RNAi* p = 0.0324, one-way Anova test. **(D)** Extracted *D. melanogaster* larvae brains from w^{1118}, *PatroninRNAi*, *WDR62RNAi*, *PatroninRNAi+ WDR6RNAi* and stained for Miranda and DAPI. The dotted white line highlights the shape of lobes. **(E)** Immunofluorescence from a larva brain stained for Miranda and α-tubulin. Dotted lines represent the pole-to-pole axe and the cellular axe perpendicular to the Miranda signal (spindle orientation angle). The magenta line represents the angle between the 2 axes. **(F)** Quantification of the spindle orientation angles (as determined in Fig.5E) in neuroblasts from *D. melanogaster* larvae brain lobes from w^{1118} (n= 48 cells), *PatroninRNAi* (n= 20), *WDR62RNAi* (n= 44), *PatroninRNAi+ WDR6RNAi* (n= 35) larvae, all non-significant, Kruskal-Wallis test. **(G)** Scheme of larvae turning behaviour assay: the number of larva contraction before each change in direction was determined (see Supplementary Fig5C for examples of tracking). **(H)** Quantification of the contractions before change of direction in w^{1118} (n=16 larvae), *PatroninRNAi* (n= 12), *WDR62RNAi* (n= 16), *Patronin RNAi+ WDR6RNAi* (n= 15) larvae. w^{1118} vs *PatroninRNAi*, w^{1118} vs *WDR62 RNAi* p = 0.0001, *WDR62 RNAi* vs *PatroninRNAi + WDR62RNAi* $p < 0.0001$, Kruskal-Wallis test. **(I)** Scheme of larvae fructose choice assay: the

proportion of larvae on the half containing fructose was counted after 5 minutes of free movements (See Supplementary Fig5D for examples of tracking). **(J)** Quantification of larvae number on the Fructose-containing half after 5 minutes of movements of w^{1118} (n=68 larvae), *PatroninRNAi* (n=58), *WDR62RNAi* (n=54), *PatroninRNAi+ WDR6RNAi* (n=53) larvae. w^{1118} vs *PatroninRNAi*, w^{1118} vs *WDR62RNAi* P = 0.0319, *WDR62RNAi* vs *PatroninRNAi + WDR62RNAi* P = 0.0390, Fisher's exact test. **(K)** Proposed model for the origin of primary microcephaly origin: We postulate that cells can can detect lagging chromosomes via the Aurora B activity gradient. If these lagging chromosomes are only briefly in contact with Aurora B, as is the case in many wild-type or more frequently in CAMSAP1-depleted cells (fast poleward microtubule flux speed), this may lead to a transient activation of 53BP1, but not an activation of p21. If these lagging chromosomes remain longer, as is the case in WDR62-depleted cells (slow poleward microtubule flux speed) this will lead to a rapid 53BP1 activation and p21 induction resulting in a cell cycle delay which can exhaust the neuroprogenitor cell pool. Re-equilibrating poleward microtubule flux rates by co-depleting CAMSAP1 and WDR62 prevents transient lagging chromosomes and rescues the primary microcephaly phenotype.

SUPPLEMENTARY MATERIAL

MATERIALS AND METHODS

Cell culture and drug treatments

hTert-RPE1 (ATCC: CRL-4000), hTert-RPE1-53BP1-GFP (kind gift of Réné Medema, (*57*)), hTert-RPE1 GFP-Centrin1/GFP-CENPA (kind gift from A. Khodjakov, State University of New York), and hTert-RPE1 PAGFP-α-tubulin cell lines (*58*) were cultured in Dulbecco's Modified Eagle's Medium (DMEM; Thermo Fisher Scientific: 61965-026), supplemented with 10% FCS (Labforce, S181T), 100 U/ml penicillin and 100 mg/ml streptomycin (Life, 15140122). All cells were cultured at 37°C with 5% CO2 in a humidified incubator. For live-cell imaging, cells were cultured in eight-, four-, or two-well Ibidi chambers (Vitaris) in Leibovitz's L-15 medium (Thermo Fisher Scientific, 21083027) supplemented with 10% FCS before imaging for maximum 12 h in the absence of CO_2. The following

drugs were added to the culture or imaging medium: 10 µM MG132 (Sigma Aldrich, C2211-5MG) for 30 min, 100 nM Doxorubicin (Sigma, D1515) for 12 h, 50 nM Aurora B inhibitor Barasertib (AZD1152, S1147, Selleckchem), 50 nM SiR-Tubulin (Spirochrome, SC002) for 2 h, 100 nM SiR DNA (Spirochrome, SC007) for 2 h, 100 nM SpY DNA (Spirochrome, SC101) for 5 h.

siRNA and plasmid transfections

For protein depletions, cells were transfected for 48 h in case of single depletions and 72 h in case of the double depletions with 20 nM siRNAs using Opti-MEM (Invitrogen, 31985-047) and Lipofectamine RNAiMAX (Invitrogen, 13778075) according to the manufacturer's instructions. For the double depletions, a double amount of Lipofectamine RNAiMAX was used. The medium was replaced 24 h after transfection. The following sense strands of validated siRNA duplexes were used (all Qiagen unless indicated): siASPM (*16*), 5′-GCU AUA UGU CAG CGU ACU ATT-3′; siCamsap1 (validated in Supplementary Figure 3) 5′-CAUCGAGAAGCUUAACGAATT-3′; siWDR62 (Dharmacon; (*14*)), 5′-AGA CAA AGG UGA CGA GCA C-3′; siNPL4 (*38*), 5′-CAGCCUCCUCCAACAAAUCdTdT-3'; siUBASH3B – 1 (*39*), 5′-CCGCTTAAGGATGCTAACATT-3', siUBASH3B - 2 (*39*),), 5′-AAGAGAGTTGTTCTTAGGTTA-3' mixed 1:1 and as a negative control siCTRL (AllStars Negative Control siRNA; Qiagen, 1027281, Proprietary).

Immunofluorescence

To stain for WDR62, 53BP1, P21, yH2AX, AuroraB, NPL4, UBASH3B hTert-RPE1 cells were fixed at -20°C for 7 min with ice-cold methanol stored at -20°C. To stain for CAMSAP1, MCAK, hTert-RPE1 cells were fixed at room temperature for 15 minutes with a solution containing 4% Formaldehyde (Applichem, A3592), 2mM of PIPES (Applichem, A1079.0500), pH 6.8, 1mM of EGTA (Applichem, A0878.0100), and 0.2% –Triton X-100 (Applichem, A4975.0100). To stain for α-tubulin cells were washed 30 seconds in a 37°C warm buffer containing 80mM M KOH-PIPES, 10mM MgCl2 (Applichem, 131396.1211), 5mM EGTA, 0.5% Triton-X and fixed at room temperature for 10 minutes in a 12.5% Glutaraldehyde (Sigma Aldrich, G5882), 80mM KOH-PIPES, 10mM MgCl2, 5mM EGTA and 0.5% Triton-X solution. Cells were washed for 7 minutes in a freshly prepared 0.1% NaBH4 (Sigma Aldrich, 16940-66-2) in PBS quenching solution. The samples were washed twice for 2 minutes in PBS.

After all fixations cells were rinsed with PBS and blocked 1 hour in blocking buffer (PBS + 3% BSA (LabForce, S181T) and 1% N3Na (Applichem, A1430). After blocking, cells were washed thrice for 5 minutes with PBS and incubated 1 hour with the primary antibody diluted in blocking buffer. Next, cells were washed twice in PBS and incubated 1 hour with the secondary antibody diluted in blocking buffer. Coverslips were mounted on microscopes slides with DAPI Vectashield mounting medium (Vector Laboratories, H1200).

The following primary antibodies were used: recombinant human anti-α-tubulin (1:500; (*59*)), rabbit anti-CAMSAP1(1:1500; Novus Biologicals NBP1-26645), rabbit anti-WDR62 (1:1000; Bethyl A301-560A), rabbit anti-MCAK (1:1000; (*60*)), rabbit anti-53BP1 (1:1000; Cell Signalling Technology 4937), mouse anti-p21 (1:1000; Cell Signalling Technology 2947), mouse anti-yH2Ax (1:2000; EMD Millipore, 05-636), mouse anti-AuroraB (1:2000; BD Biosciences 611083), rabbit anti-NPL4(1:500; Novus Biologicals NBP1-82166), rabbit anti-UBASH3B (1:500; Proteintech 19563-1-AP). For secondary antibodies, Alexa Fluor–conjugated antibodies (1:400; Invitrogen) were used. The pictures used for the analysis were acquired using 60× and 100× (NA 1.4) oil objectives on Olympus DeltaVision wide-field microscope (GE Healthcare) equipped with a DAPI/FITC/TRITC/Cy5 filter set (Chroma Technology Corp.) and Coolsnap HQ2 CCD camera (Roper Scientific) running Softworx (GE Healthcare). Alternatively, they were also acquired using a HC PL APO CS2 63x/1.40 Oil objective on a Leica Stellaris 5 confocal microscope equipped with 405 nm, 488nm, 561nm and 638 nm lasers and two Hybrid S detectors (HyD S1 and HyD S2) running LAS X software (version: 4.5.0.25531).

Live-cell imaging

To monitor mitotic progression and chromosome segregation, hTert-RPE1 and hTert-RPE1-53BP1 GFP cells were seeded into Ibidi chambers (Vitaris) and treated with siRNAs, supplemented with imaging medium 2–3 h before imaging and recorded on a Nikon Eclipse Ti-E wide-field microscope (Nikon) equipped with a GFP/mCherry/Cy5 filter set (Chroma Technology Corp.), an Orca Flash 4.0 complementary metal-oxide-semiconductor camera (Hamamatsu), and an environmental chamber using NIS software (Nikon). Cells were imaged in the GFP and Cy5 channels for 12 h at 37°C, at 1-

min 30 sec or 2 min intervals, in 17 steps of 1 µm Z-stacks, using a 60× (NA 1.51) oil objective and 2 × 2 binning.

Anaphase kinetochore tracking assay

hTert-RPE1 GFP-centrin1/GFP-CENPA (kind gift of Alexey Khodjakov) were treated with the reported siRNAs, and metaphase cells imaged for 15 min every 15 s using a 100× (NA 1.4) oil objective on an Olympus DeltaVision wide-field microscope (GE Healthcare) equipped with an environmental chamber maintained at 37°C and a GFP/RFP filter set (Chroma Technology Corp.). Z-stacks of 15-µm thickness with z-slices separated by 0.5 µm were imaged in the GFP channel with 2 × 2 binning to track kinetochores from metaphase until late anaphase. 4D images (XYZT) obtained were deconvolved in conservative mode and cropped using Softworx (GE Healthcare). The kinetochores and the poles were segmented using Imaris (Bitplane) during metaphase and anaphase. The kinetochores positions over time were analysed using a Matlab code ((*14*), https://github.com/AmandaGuerreiro/WDR62_2020).

Poleward microtubule flux measurement

hTert-RPE1 PA-GFP-α-tubulin cells were incubated with 10 µM MG132 for 30 minutes and imaged for 1 hour. Single focal planes of 150-nm pixel size were acquired using a 60× (NA 1.4) CFI Plan Apochromat oil objective on a Nikon A1r point scanning confocal microscope equipped with a 37°C heating chamber and running NIS elements software. A 3-pixel-thick and 100-pixel-long ROI parallel to the DNA and close to spindle centre was photoactivated with a 500-ms, 405-nm laser pulse at 50–100% intensity depending on the PA-GFP-α-tubulin expression levels and imaged every 20 seconds for 4 min in a single focal plane. The photoactivated mark was tracked manually for 120 s with Fiji (ImageJ). Distance between the photoactivated mark and the corresponding spindle pole was tracked in time and the displacement of the photoactivated mark over time was calculated.

Metaphase spreads

Cells were incubated with 1mM Nocodazole (Sigma Aldrich, M1404-2MG) for 1h at 37C. Mitotic cells were shaken off, centrifuged and resuspended in 0.56% KCl (Applichem, A3582.0500) at room temperature for 6 min, before resuspending them dropwise in a 5 ml 3:1 MeOH/ CH3COOH

(AppliChem, A2369) solution. The excess of supernatant was removed and 20ul of cells suspension was dropwise added on the cooled microscopy slide (Epredia, 1.0mm) and left to dry in humid air chamber for at least 1h. The metaphase spreads were then mounted using DAPI Vectashield and Epredia cover slips 22x22 mm.

CFSE labelling for cell proliferation assay

Cells were trypsinized, centrifuged, washed once with PBS, and resuspended in PBS at a concentration of 1×10^6 cells/ml in the presence of 1 μM CFSE (BioLegend, 423801) for 20 min at 37 °C. The CFSE was quenched by adding 5 times the original staining volume of cell culture medium for 10 min. After a final washing step, a fraction of the cells was resuspended in PBS with 20mM Tris (Applichem, A1379.5000) and 0.1% FCS and quantified by flow cytometry for reference (see below). The remaining cells was seeded and treated with siRNAs for 5 days. After 5 days of incubation, CFSE signal intensity was measured using 488 nm laser on Beckman Coulter Cytoflex.

Image processing and 53BP1, p21 and γH2AX quantifications

Immunofluorescence images were first converted to z-stack (sum slices) using ImageJ/Fiji and opened in QuPath 0.4.3 (*61*). To quantify 53BP1, p21 or γH2AX, nuclei were segmented using the DAPI channel. To detect 53BP1 foci, a code was used to determine foci with a minimal area of 0.2 μm^2 and an intensity higher than the mean nuclear intensity plus 2 standard deviations. For p21 or γH2AX intensities, an automatized QuPath analysis was used to analyse p21 or γH2AX levels in segmented nuclei. The background was subtracted, and cells were counted as positive if their intensity was higher than the mean plus one standard deviation of the intensity in *siCTRL*-treated cells. Time-lapse movies were analysed manually with NIS Elements software to quantify mitotic timing and presence of 53BP1 foci, taking into account cells 4h after mitosis. Time-lapse movies were also analysed manually with NIS Elements software to quantify the presence or absence of transient lagging chromosomes. These were quantified as present when DNA clouds in anaphase were > 6um apart and the lagging was > 2um long. For siRNA immunofluorescence quantification, 3D images were analysed manually with

ImageJ/Fiji. Aurora B intensity in anaphase was quantified using surface tool on DNA signal Imaris (Bitplane) 10.

All the data were plotted using GraphPad Prism 8.2.1.

***D. melanogaster* strains**

The following sources of different D. melanogaster lines were used in this study:

Source	Strain	ID
Régis Giet lab	*w*; InscuteableGal4/Cyo (II)	Bloomington *Drosophila* Stock centre: 8751
NIG-Fly	*w*; UAS-Wdr62-RNAi (III)	7337-R1
VDRC	*w*; UAS-Patronin--RNAi (II)	108927
Emi Nagoshi lab	w^{1118} -/-	

D. melanogaster fruit flies were raised at 25 °C in the standard medium.

Immunofluorescence of *D. melanogaster* brain larvae

3rd instar larvae were collected 120h after an egg laying of 5h. Larval brains were dissected in testis buffer (TB, 183 mM KCl, 47 mM NaCl, 10 mM Tris, and 1 mM EDTA, pH 6.8 MT) and brains were fixed at room temperature for 20 min in TB + 10% FA and 0.01% Triton-X. Brains were washed 2 times x 15 minutes in PBS and then 2 times x 15 minutes in PBS + 0.1% Triton-X. Brains were blocked for 1 hour in PBSTB (1% BSA, 0.1% Triton-X in PBS). Brains were incubated with the primary antibodies in PBSTB for 1 hour at room temperature. After 1 wash with PBS, brains were incubated with secondary antibodies in PBSTB for 1 hour at room temperature. After washes, samples were mounted on microscope slides with DAPI Vectashield mounting medium (to avoid brain deformation, for brain size measurements, spacer were used while mounting microscope slides).

The following primary antibody was used: rat anti-Miranda (1:500, Abcam, ab197788). For secondary antibodies, Alexa Fluor–conjugated antibodies (1:400; Invitrogen) were used. For neuroblast counting

and spindle orientation experiments, images were acquired using a HC PL APO CS2 40x/1.40 air objective on a Leica stellaris 5 confocal microscope equipped with 405 nm, 488nm, 561nm and 638 nm lasers and two Hybrid S detectors (HyD S1 and HyD S2) running LAS X software (version: 4.5.0.25531). For brain size image acquisitions, a Nikon Eclipse Ti-E wide-field microscope (Nikon) equipped with a GFP/mCherry filter set (Chroma Technology Corp.), an Orca Flash 4.0 complementary metal-oxide-semiconductor camera (Hamamatsu), and an environmental chamber using NIS software (Nikon) was used.

To measure brain lobe sizes, the average diameter of one brain lobe was calculated as the mean of two measurements in orthogonal orientation (length + width / 2) using Fiji. The brain lobe shape was approximated to a circle shape and the area was calculated with the formula: *Area=(π diameter^2)/4*

The number of neuroblasts in the central brain was calculated as the number of Miranda positive cells, manually using FIJI, and the average of the two lobes was reported. For spindle orientation, Fiji from ImageJ software was used to calculate the angle between the spindle poles axis and a line perpendicular to Miranda signal.

Cognitive tests

For running assay, all 3rd instar larvae were recorded directly after collection on a 0.8% agar 10 cm (500 ml water, 4 g agar (Roth, Karlsruhe)) surface. Prior to recording, larvae were briefly washed with PBS. Turning frequency is indicated as the number of peristaltic movements a larva needs to make before turning. Movies of 5 min were made and analysed by hand selecting a 1 min interval. For fructose assay, all 3rd instar larvae were recorded directly after collection on a 0.8% agar 10 cm (500 ml water, 4 g agar (Roth, Karlsruhe)) surface, containing in one half 0.2M Fructose (Sigma Aldrich, F0127, 3.6g in 100 ml 0.8% agar) and no fructose in the other half. Prior to recording, larvae were briefly washed with PBS. Fructose preference was evaluated by setting the larvae in the middle of the dish and allowing them to choose a side. The movements were recorded, and the final choice was analysed by the end of 5 min.

SUPPLEMENTARY FIGURE LEGENDS

Supplementary Figure 1: WDR62 depletion, and quantification of γH2AX, 53BP1 and p21 (**A**) Immunofluorescence images of metaphase RPE1 cells treated with *siCTRL* and *siWDR62* and stained with DAPI and WDR62 antibodies. Scale bars = 5 µm. (**B**) Quantification of WDR62 levels in RPE1 cells treated with *siCTRL* or *siWDR62* cells normalized to *siCTRL* values. N = 4 independent experiments, n = 49-81 cells, ****, $p < 0.0001$, unpaired t-test. Error bars represent SEM. (**C**) Live stills of GFP-centrin1/GFP-CENP-A RPE1 anaphase cells treated with *siCTRL* or *siWDR62*. White arrow indicates transient lagging chromosome in *siWDR62*-treated cell. (**D**) Quantification of GFP-Centrin1/GFP-CENP-A RPE1 cells with transient lagging chromosomes in anaphase after *siCTRL or siWDR62* treatment. n = 29-48 cells; * $p = 0.0317$ in Fischer's exact test. Note that the data represented here are a duplicate of the quantification in Figure 3L. (**E**) Schematic representation of automated 53BP1 (upper panel) and p21/yH2AX analysis (lower panel). Nuclei were segmented using DAPI staining, and, for 53BP1, foci were counted as positive if the spots displayed an intensity than was higher than the nuclear mean plus 2 standard deviations; for p21/yH2AX the intensity of nuclei in corresponding channel were measured and counted as positive if their intensity was higher than the mean plus one standard deviation in *siCTRL*-treated cells. (**F**) Immunofluorescence images of interphase RPE1 cells, treated with *siCTRL*, *siWDR62* or 100 nM Doxorubicin, stained with DAPI and γH2AX antibody. Blue dotted circles represent γH2AX-negative nuclei, red ones γH2AX-positive nuclei. Scale bars = 10 µm. (**G**) Quantification of yH2AX positive cells after *siCTRL, siWDR62* or Doxorubicin treatment. N = 6, n = 834 – 2234 cells; *siCTRL* vs. Doxorubicin, ****, $p < 0.0001$, Fisher's exact test. (**H**) Schematic representation the Carboxyfluorescein succinimidyl ester (CFSE) assay: CFSE is a cell-permeable dye that covalently couples to intramolecular molecules via its succinimidyl group; since after a CFSE pulse its intensity decreases by half after each cell division, it can be used as a pulse-chase assay to quantify cell proliferation. In all our assays we compared the indicated siRNA-treatments to serum starvation. To calculate the number of cell divisions above serum starvation we determined by FACS the peak intensity of a serum-starved cells (A) and divided it by the peak intensity

of the condition of interest (X). The log2 of (A/X) indicates the number of additional divisions cells have undergone in comparison to serum-starvation.

Supplementary figure 2: ASPM, NPL4, UBASH3B siRNA validation and characterization (A) Immunofluorescence images of RPE-1 cells treated with *siCTRL* or *siASPM*, and stained for ASPM and DAPI. **(B)** Quantification of ASPM levels in RPE-1 cells treated with *siCTRL* and *siASPM*. ASPM intensity was normalized to *siCTRL* in each replicate. N = 3, n = 26-40 cells; **** $p < 0.0001$, student t-test. **(C)** Immunofluorescence images of RPE-1 cells treated with *siCTRL* or *siNPL4* stained for NPL4 and DAPI. **(D)** Quantification of NPL4 levels in RPE-1 cells treated with *siCTRL* or *siNPL4*. NPL4 intensity was normalized to *siCTRL* in each replicate. N = 3, n = 419-430 cells; **** $P < 0.0001$, student t-test. **(E)** Immunofluorescence images of RPE-1 cells treated with *siCTRL* or *siUBASH3B* stained for UBASH3B and DAPI. **(F)** Quantification of UBASH3B levels in RPE-1 cells treated with *siCTRL* or *siUBASH3B*. UBASH3B intensity was normalized to *siCTRL* in each replicate. N =3, n = 429-442 cells; $p < 0.0001$, student t-test. **(G and H)** Quantification of mitotic timing of RPE-1 cells treated with *siCTRL*, (G) *siNPL4* or (H) *siUBASH3B*, based on SiR-DNA live cell movies. Mitotic time is calculated from nuclear envelope break down till anaphase onset. N = 3, n = 39-90 cells. ns in student t-test**(I)** Quantification of transient lagging chromosomes in live PRE-1 cells stained with SiR-DNA and treated with *siCTRL*, *siNPL4* or *siUBASH3B*. ns in Fisher's exact test. **(J)** immunofluorescence image of RPE-1 cells treated with DMSO (CTRL), Barasetrib and stained for MCAK and DAPI. **(K)** Quantification of MCAK levels on kinetochores in RPE-1 cells treated with DMSO (CTRL) and Barasertib. MCAK intensity was measured on 10 kinetochores randomly selected per cell, MCAK values were normalized on the average intensity of the CTRL in each replicate. N=3 replicates, n = 438-458 kinetochores, **** $P < 0.0001$, student t-test. All scale bars = 5 mm.

Supplementary figure 3: (A) *D. melanogaster* larva brain scheme, **(B)** *D. melanogaster* crosses used for the experiments reported in Figure 5. Wild-type (w^{1118}), *PatroninRNAi*, *WDR62RNAi*, *PatroninRNAi+ WDR6RNAi* flies were crossed with *InscGAL4* flies in order to obtain larvae expressing the RNAi in type I and type II neuroblasts. **(C and D)** Examples of tracking of w^{1118}, *PatroninRNAi*, *WDR62RNAi*, *PatroninRNAi+ WDR6RNAi* larvae movements on agar plates. Each colour is a single

larva tracking. In (D) the agar plates are composed of a half agar Fructose+ and the other half agar Fructose-.

REFERENCES

1. D. Jayaraman, B.-I. Bae, C. A. Walsh, The Genetics of Primary Microcephaly. *Annu. Rev. Genom. Hum. Genet.* **19**, 1–24 (2018).

2. R. S. O'Neill, T. A. Schoborg, N. M. Rusan, Same but different: pleiotropy in centrosome-related microcephaly. *Mol. Biol. Cell* **29**, 241–246 (2018).

3. E. A. Nigg, L. Čajánek, C. Arquint, The centrosome duplication cycle in health and disease. *FEBS letters* **588**, 2366–2372 (2014).

4. M. Nano, R. Basto, Cell Division Machinery and Disease. *Adv. Exp. Med. Biol.* **1002**, 19–45 (2017).

5. T. P. Phan, A. J. Holland, Time is of the essence: the molecular mechanisms of primary microcephaly. *Genes Dev.* **35**, 1551–1578 (2021).

6. V. Marthiens, M. A. Rujano, C. Pennetier, S. Tessier, P. Paul-Gilloteaux, R. Basto, Centrosome amplification causes microcephaly. *Nature cell biology* **15**, 731–740 (2013).

7. C.-T. Chen, H. Hehnly, Q. Yu, D. Farkas, G. Zheng, S. D. Redick, H.-F. Hung, R. Samtani, A. Jurczyk, S. Akbarian, C. Wise, A. Jackson, M. Bober, Y. Guo, C. Lo, S. Doxsey, A Unique Set of Centrosome Proteins Requires Pericentrin for Spindle-Pole Localization and Spindle Orientation. *Curr. Biol.* **24**, 2327–2334 (2014).

8. S. B. Lizarraga, S. P. Margossian, M. H. Harris, D. R. Campagna, A.-P. Han, S. Blevins, R. Mudbhary, J. E. Barker, C. A. Walsh, M. D. Fleming, Cdk5rap2 regulates centrosome function and chromosome segregation in neuronal progenitors. *Development* **137**, 1907–1917 (2010).

9. J. L. Fish, Y. Kosodo, W. Enard, S. Pääbo, W. B. Huttner, Aspm specifically maintains symmetric proliferative divisions of neuroepithelial cells. *Proceedings of the National Academy of Sciences of the United States of America* **103**, 10438–10443 (2006).

10. T. P. Phan, A. L. Maryniak, C. A. Boatwright, J. Lee, A. Atkins, A. Tijhuis, D. C. Spierings, H. Bazzi, F. Foijer, P. W. Jordan, T. H. Stracker, A. J. Holland, Centrosome defects cause microcephaly by activating the 53BP1-USP28-TP53 mitotic surveillance pathway. *EMBO J.* **40**, e106118 (2021).

11. S. Rasool, J. M. Baig, A. Moawia, I. Ahmad, M. Iqbal, S. S. Waseem, M. Asif, U. Abdullah, E. U. H. Makhdoom, E. Kaygusuz, M. Zakaria, S. Ramzan, S. ul Haque, A. Mir, I. Anjum, M. Fiaz, Z. Ali, M. Tariq, N. Saba, W. Hussain, B. Budde, S. Irshad, A. A. Noegel, S. Höning, S. M. Baig, P. Nürnberg, M. S. Hussain, An update of pathogenic variants in ASPM, WDR62, CDK5RAP2, STIL, CENPJ, and CEP135 underlying autosomal recessive primary microcephaly in 32 consanguineous families from Pakistan. *Mol. Genet. Genom. Med.* **8**, e1408 (2020).

12. J. N. Pulvers, J. Bryk, J. L. Fish, M. Wilsch-Bräuninger, Y. Arai, D. Schreier, R. Naumann, J. Helppi, B. Habermann, J. Vogt, R. Nitsch, A. Tóth, W. Enard, S. Pääbo, W. B. Huttner, Mutations in

mouse Aspm (abnormal spindle-like microcephaly associated) cause not only microcephaly but also major defects in the germline. *Proc. Natl. Acad. Sci.* **107**, 16595–16600 (2010).

13. E. A. Tungadi, A. Ito, T. Kiyomitsu, G. Goshima, Human microcephaly ASPM protein is a spindle pole-focusing factor that functions redundantly with CDK5RAP2. *J. Cell Sci.* **130**, 3676–3684 (2017).

14. A. Guerreiro, F. D. Sousa, N. Liaudet, D. Ivanova, A. Eskat, P. Meraldi, WDR62 localizes katanin at spindle poles to ensure synchronous chromosome segregation. *J Cell Biol* **220**, e202007171 (2021).

15. J. Huang, Z. Liang, C. Guan, S. Hua, K. Jiang, WDR62 regulates spindle dynamics as an adaptor protein between TPX2/Aurora A and katanin. *J Cell Biology* **220**, e202007167 (2021).

16. K. Jiang, L. Rezabkova, S. Hua, Q. Liu, G. Capitani, A. F. M. Altelaar, A. J. R. Heck, R. A. Kammerer, M. O. Steinmetz, A. Akhmanova, Microtubule minus-end regulation at spindle poles by an ASPM–katanin complex. *Nat Cell Biol* **19**, 480–492 (2017).

17. M. Barisic, G. Rajendraprasad, Y. Steblyanko, The metaphase spindle at steady state – Mechanism and functions of microtubule poleward flux. *Semin Cell Dev Biol* **117**, 99–117 (2021).

18. G. A. Pavlova, A. V. Razuvaeva, J. V. Popova, E. N. Andreyeva, L. A. Yarinich, M. O. Lebedev, C. Pellacani, S. Bonaccorsi, M. P. Somma, M. Gatti, A. V. Pindyurin, The role of Patronin in Drosophila mitosis. *Bmc Mol Cell Biology* **20**, 7 (2019).

19. M. C. Hendershott, R. D. Vale, Regulation of microtubule minus-end dynamics by CAMSAPs and Patronin. *Proc National Acad Sci* **111**, 5860–5865 (2014).

20. S. S. Goodwin, R. D. Vale, Patronin Regulates the Microtubule Network by Protecting Microtubule Minus Ends. *Cell* **143**, 263–274 (2010).

21. K. Jiang, S. Hua, R. Mohan, I. Grigoriev, K. W. Yau, Q. Liu, E. A. Katrukha, A. F. M. Altelaar, A. J. R. Heck, C. C. Hoogenraad, A. Akhmanova, Microtubule Minus-End Stabilization by Polymerization-Driven CAMSAP Deposition. *Dev. Cell* **28**, 295–309 (2014).

22. J. Atherton, K. Jiang, M. M. Stangier, Y. Luo, S. Hua, K. Houben, J. J. E. van Hooff, A.-P. Joseph, G. Scarabelli, B. J. Grant, A. J. Roberts, M. Topf, M. O. Steinmetz, M. Baldus, C. A. Moores, A. Akhmanova, A structural model for microtubule minus-end recognition and protection by CAMSAP proteins. *Nat. Struct. Mol. Biol.* **24**, 931–943 (2017).

23. O. Sen, J. U. Harrison, N. J. Burroughs, A. D. McAinsh, Kinetochore life histories reveal an Aurora-B-dependent error correction mechanism in anaphase. *Dev. Cell* **56**, 3405 (2021).

24. E. P. Rogakou, D. R. Pilch, A. H. Orr, V. S. Ivanova, W. M. Bonner, DNA double-stranded breaks induce histone H2AX phosphorylation on serine 139. *J. Biol. Chem.* **273**, 5858–68 (1998).

25. L. B. Schultz, N. H. Chehab, A. Malikzay, T. D. Halazonetis, P53 Binding Protein 1 (53bp1) Is an Early Participant in the Cellular Response to DNA Double-Strand Breaks. *J. Cell Biol.* **151**, 1381–1390 (2000).

26. Y. Uetake, G. Sluder, Prolonged prometaphase blocks daughter cell proliferation despite normal completion of mitosis. *Current biology : CB* **20**, 1666–1671 (2010).

27. B. G. Lambrus, V. Daggubati, Y. Uetake, P. M. Scott, K. M. Clutario, G. Sluder, A. J. Holland, A USP28–53BP1–p53–p21 signaling axis arrests growth after centrosome loss or prolonged mitosis. *J. Cell Biol.* **214**, 143–153 (2016).

28. F. Meitinger, J. V. Anzola, M. Kaulich, A. Richardson, J. D. Stender, C. Benner, C. K. Glass, S. F. Dowdy, A. Desai, A. K. Shiau, K. Oegema, 53BP1 and USP28 mediate p53 activation and G1 arrest after centrosome loss or extended mitotic duration. *J. Cell Biol.* **214**, 155–166 (2016).

29. C. S. Fong, G. Mazo, T. Das, J. Goodman, M. Kim, B. P. O'Rourke, D. Izquierdo, M.-F. B. Tsou, 53BP1 and USP28 mediate p53-dependent cell cycle arrest in response to centrosome loss and prolonged mitosis. *eLife* **5**, e16270 (2016).

30. W. S. El-Deiry, T. Tokino, V. E. Velculescu, D. B. Levy, R. Parsons, J. M. Trent, D. Lin, W. E. Mercer, K. W. Kinzler, B. Vogelstein, WAF1, a potential mediator of p53 tumor suppression. *Cell* **75**, 817–825 (1993).

31. S. L. Thompson, D. A. Compton, Proliferation of aneuploid human cells is limited by a p53-dependent mechanism. *J Cell Biol* **188**, 369–381 (2010).

32. S. Santaguida, A. Tighe, A. M. D'Alise, S. S. Taylor, A. Musacchio, Dissecting the role of MPS1 in chromosome biorientation and the spindle checkpoint through the small molecule inhibitor reversine. *J Cell Biol* **190**, 73–87 (2010).

33. G. Lukinavičius, C. Blaukopf, E. Pershagen, A. Schena, L. Reymond, E. Derivery, M. Gonzalez-Gaitan, E. D'Este, S. W. Hell, D. W. Gerlich, K. Johnsson, SiR-Hoechst is a far-red DNA stain for live-cell nanoscopy. *Nature communications* **6**, 8497 (2015).

34. O. Afonso, I. Matos, A. J. Pereira, P. Aguiar, M. A. Lampson, H. Maiato, Feedback control of chromosome separation by a midzone Aurora B gradient. *Science (New York, NY)*, 1251121 (2014).

35. K. Ramadan, R. Bruderer, F. M. Spiga, O. Popp, T. Baur, M. Gotta, H. H. Meyer, Cdc48/p97 promotes reformation of the nucleus by extracting the kinase Aurora B from chromatin. *Nature* **450**, 1258–1262 (2007).

36. B. G. Fuller, M. A. Lampson, E. A. Foley, S. Rosasco-Nitcher, K. V. Le, P. Tobelmann, D. L. Brautigan, P. T. Stukenberg, T. M. Kapoor, Midzone activation of aurora B in anaphase produces an intracellular phosphorylation gradient. *Nature* **453**, 1132–1136 (2008).

37. E. H. Hinchcliffe, C. A. Day, K. B. Karanjeet, S. Fadness, A. Langfald, K. T. Vaughan, Z. Dong, Chromosome missegregation during anaphase triggers p53 cell cycle arrest through histone H3.3 Ser31 phosphorylation. *Nat. Cell Biol.* **18**, 668–675 (2016).

38. G. Dobrynin, O. Popp, T. Romer, S. Bremer, M. H. A. Schmitz, D. W. Gerlich, H. Meyer, Cdc48/p97–Ufd1–Npl4 antagonizes Aurora B during chromosome segregation in HeLa cells. *J. Cell Sci.* **124**, 1571–1580 (2011).

39. K. Krupina, C. Kleiss, T. Metzger, S. Fournane, S. Schmucker, K. Hofmann, B. Fischer, N. Paul, I. M. Porter, W. Raffelsberger, O. Poch, J. R. Swedlow, L. Brino, I. Sumara, Ubiquitin Receptor Protein UBASH3B Drives Aurora B Recruitment to Mitotic Microtubules. *Dev. Cell* **36**, 63–78 (2016).

40. W. Lan, X. Zhang, S. L. Kline-Smith, S. E. Rosasco, G. A. Barrett-Wilt, J. Shabanowitz, D. F. Hunt, C. E. Walczak, P. T. Stukenberg, Aurora B Phosphorylates Centromeric MCAK and Regulates Its Localization and Microtubule Depolymerization Activity. *Curr. Biol.* **14**, 273–286 (2004).

41. F. Calegari, W. B. Huttner, An inhibition of cyclin-dependent kinases that lengthens, but does not arrest, neuroepithelial cell cycle induces premature neurogenesis. *J. Cell Sci.* **116**, 4947–4955 (2003).

42. A. R. Nair, P. Singh, D. S. Garcia, D. Rodriguez-Crespo, B. Egger, C. Cabernard, The Microcephaly-Associated Protein Wdr62/CG7337 Is Required to Maintain Centrosome Asymmetry in Drosophila Neuroblasts. *Cell reports*, doi: 10.1016/j.celrep.2015.12.097 (2016).

43. A. H. Brand, N. Perrimon, Targeted gene expression as a means of altering cell fates and generating dominant phenotypes. *Development* **118**, 401–415 (1993).

44. E. Derivery, C. Seum, A. Daeden, S. Loubéry, L. Holtzer, F. Jülicher, M. Gonzalez-Gaitan, Polarized endosome dynamics by spindle asymmetry during asymmetric cell division. *Nature* **528**, 280–285 (2015).

45. N. R. Lim, B. Shohayeb, O. Zaytseva, N. Mitchell, S. S. Millard, D. C. H. Ng, L. M. Quinn, Glial-Specific Functions of Microcephaly Protein WDR62 and Interaction with the Mitotic Kinase AURKA Are Essential for Drosophila Brain Growth. *Stem Cell Rep.* **9**, 32–41 (2017).

46. S. X. Atwood, K. E. Prehoda, aPKC Phosphorylates Miranda to Polarize Fate Determinants during Neuroblast Asymmetric Cell Division. *Curr. Biol.* **19**, 723–729 (2009).

47. W. Song, M. Onishi, L. Y. Jan, Y. N. Jan, Peripheral multidendritic sensory neurons are necessary for rhythmic locomotion behavior in Drosophila larvae. *Proc. Natl. Acad. Sci.* **104**, 5199–5204 (2007).

48. J. Bittern, M. Praetz, M. Baldenius, C. Klämbt, Long-Term Observation of Locomotion of Drosophila Larvae Facilitates Feasibility of Food-Choice Assays. *Adv. Biol.* **6**, e2100938 (2022).

49. J.-F. Chen, Y. Zhang, J. Wilde, K. C. Hansen, F. Lai, L. Niswander, Microcephaly disease gene Wdr62 regulates mitotic progression of embryonic neural stem cells and brain size. *Nature communications* **5**, 3885 (2014).

50. F. Meitinger, H. Belal, R. L. Davis, M. B. Martinez, A. K. Shiau, K. Oegema, A. Desai, Control of cell proliferation by memories of mitosis. *Sci. (N. York, NY)* **383**, 1441–1448 (2024).

51. A. D. McAinsh, G. J. P. L. Kops, Principles and dynamics of spindle assembly checkpoint signalling. *Nat Rev Mol Cell Bio*, 1–17 (2023).

52. D. Cimini, B. J. Howell, P. S. Maddox, A. L. Khodjakov, F. Degrassi, E. D. Salmon, Merotelic kinetochore orientation is a major mechanism of aneuploidy in mitotic mammalian tissue cells. *J Cell Biol* **153**, 517–527 (2001).

53. B. Orr, F. D. Sousa, A. M. Gomes, O. Afonso, L. T. Ferreira, A. C. Figueiredo, H. Maiato, An anaphase surveillance mechanism prevents micronuclei formation from frequent chromosome segregation errors. *Cell Reports* **37**, 109783 (2021).

54. H. Maiato, S. Silva, Double-checking chromosome segregation. *J Cell Biology* **222**, e202301106 (2023).

55. C. L. Fonseca, H. L. H. Malaby, L. A. Sepaniac, W. Martin, C. Byers, A. Czechanski, D. Messinger, M. Tang, R. Ohi, L. G. Reinholdt, J. Stumpff, Mitotic chromosome alignment ensures mitotic fidelity by promoting interchromosomal compaction during anaphase. *J. Cell Biol.* **218**, 1148–1163 (2019).

56. S. Matsuura, Y. Matsumoto, K. Morishima, H. Izumi, H. Matsumoto, E. Ito, K. Tsutsui, J. Kobayashi, H. Tauchi, Y. Kajiwara, S. Hama, K. Kurisu, H. Tahara, M. Oshimura, K. Komatsu, T. Ikeuchi, T. Kajii, Monoallelic BUB1B mutations and defective mitotic-spindle checkpoint in seven families with premature chromatid separation (PCS) syndrome. *Am. J. Méd. Genet. Part A* **140A**, 358–367 (2006).

57. A. Janssen, M. van der Burg, K. Szuhai, G. J. P. L. Kops, R. H. Medema, Chromosome Segregation Errors as a Cause of DNA Damage and Structural Chromosome Aberrations. *Science* **333**, 1895–1898 (2011).

58. A. Toso, J. R. Winter, A. J. Garrod, A. C. Amaro, P. Meraldi, A. D. McAinsh, Kinetochore-generated pushing forces separate centrosomes during bipolar spindle assembly. *J Cell Biol* **184**, 365–372 (2009).

59. A. Guerreiro, P. Meraldi, AA344 and AA345 antibodies recognize the microtubule network in human cells by immunofluorescence. *Antib Reports* **2**, e17 (2019).

60. A. C. Amaro, C. P. Samora, R. Holtackers, E. Wang, I. J. Kingston, M. C. Alonso, M. A. Lampson, A. D. McAinsh, P. Meraldi, Molecular control of kinetochore-microtubule dynamics and chromosome oscillations. *Nature cell biology* **12**, 319–329 (2010).

61. P. Bankhead, M. B. Loughrey, J. A. Fernández, Y. Dombrowski, D. G. McArt, P. D. Dunne, S. McQuaid, R. T. Gray, L. J. Murray, H. G. Coleman, J. A. James, M. Salto-Tellez, P. W. Hamilton, QuPath: Open source software for digital pathology image analysis. *Sci. Rep.* **7**, 16878 (2017).

Figure 1 Doria, Ivanova et al.

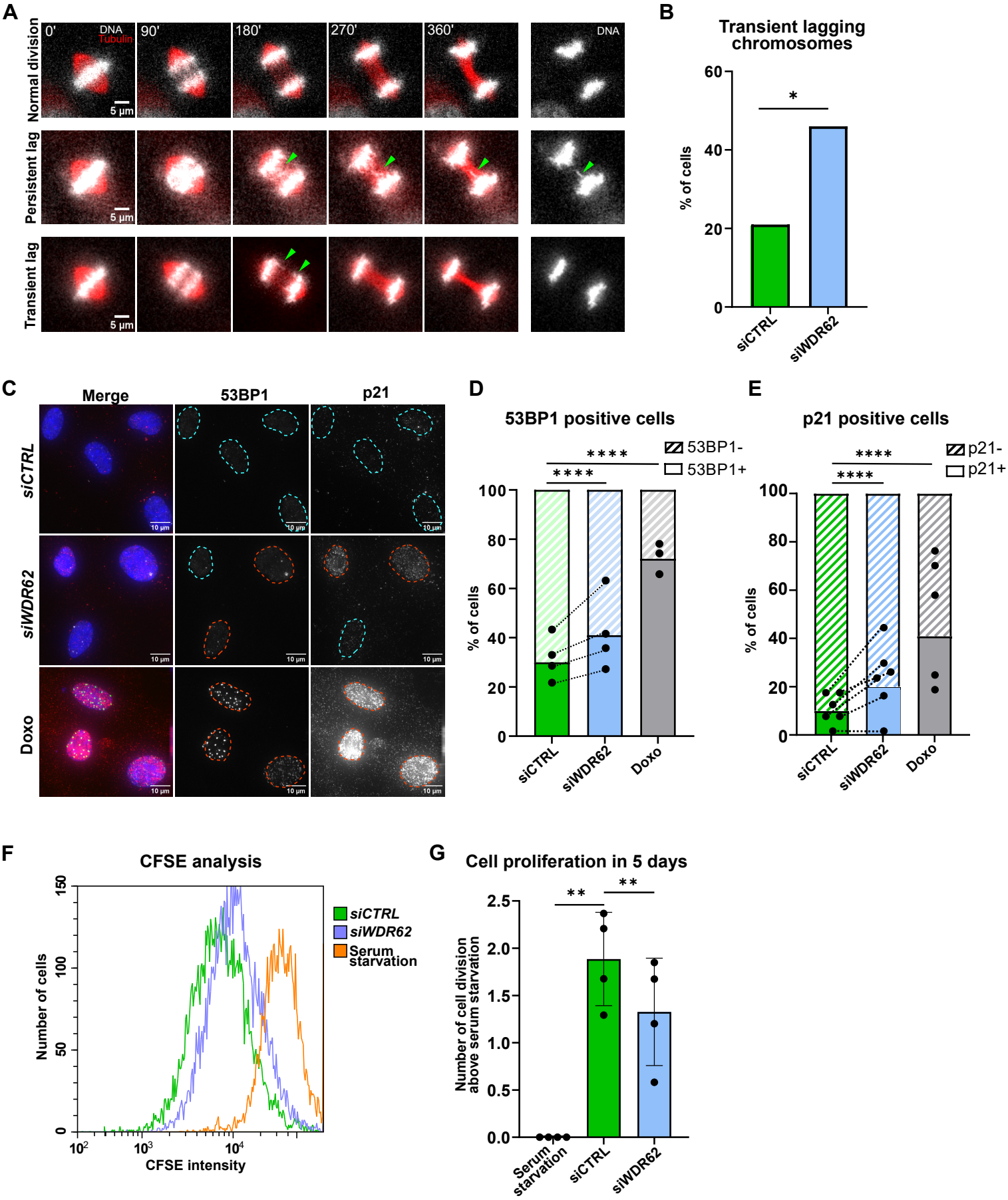

Figure 2 Doria, Ivanova et al.,

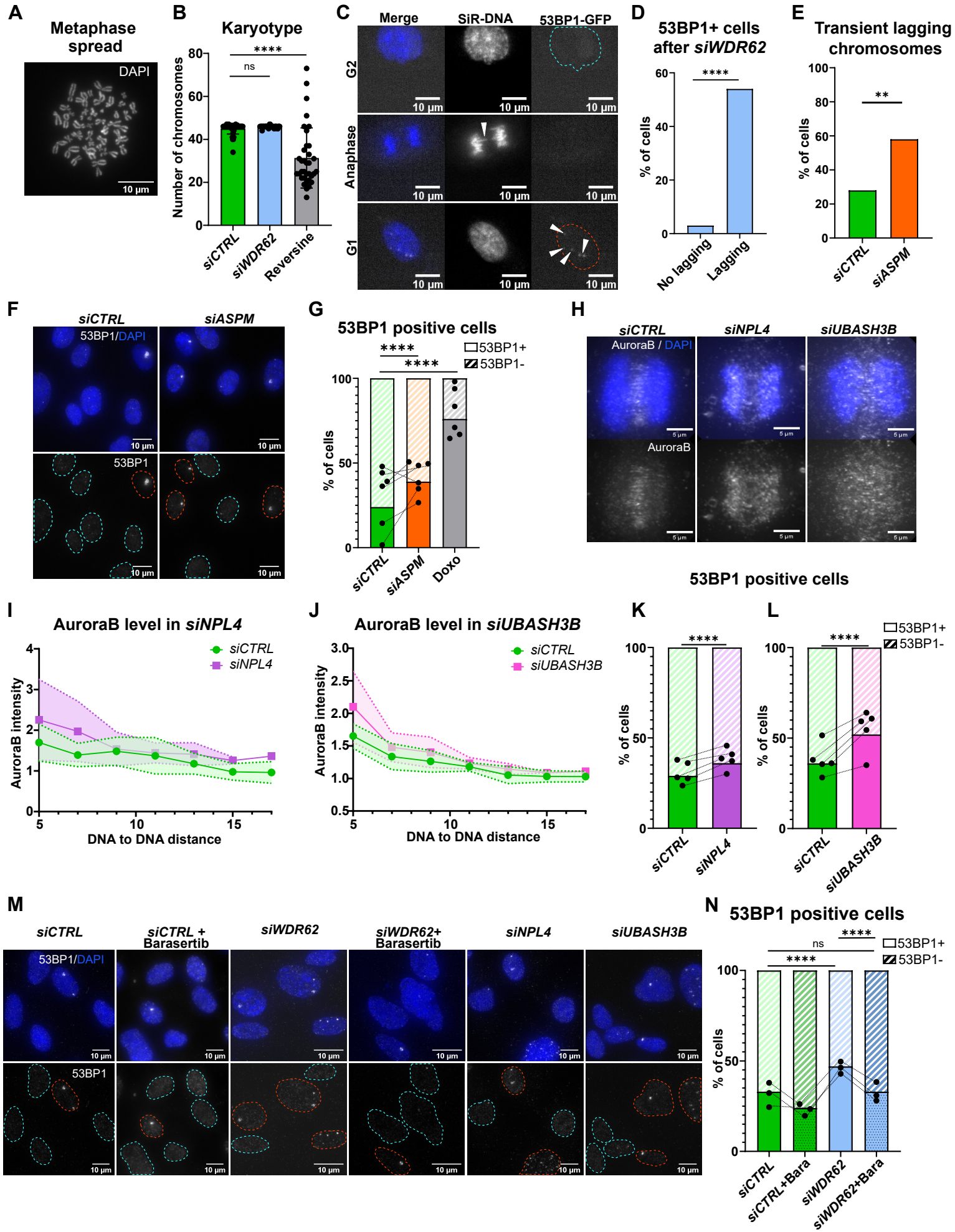

Figure 3 Doria, Ivanova et al.,

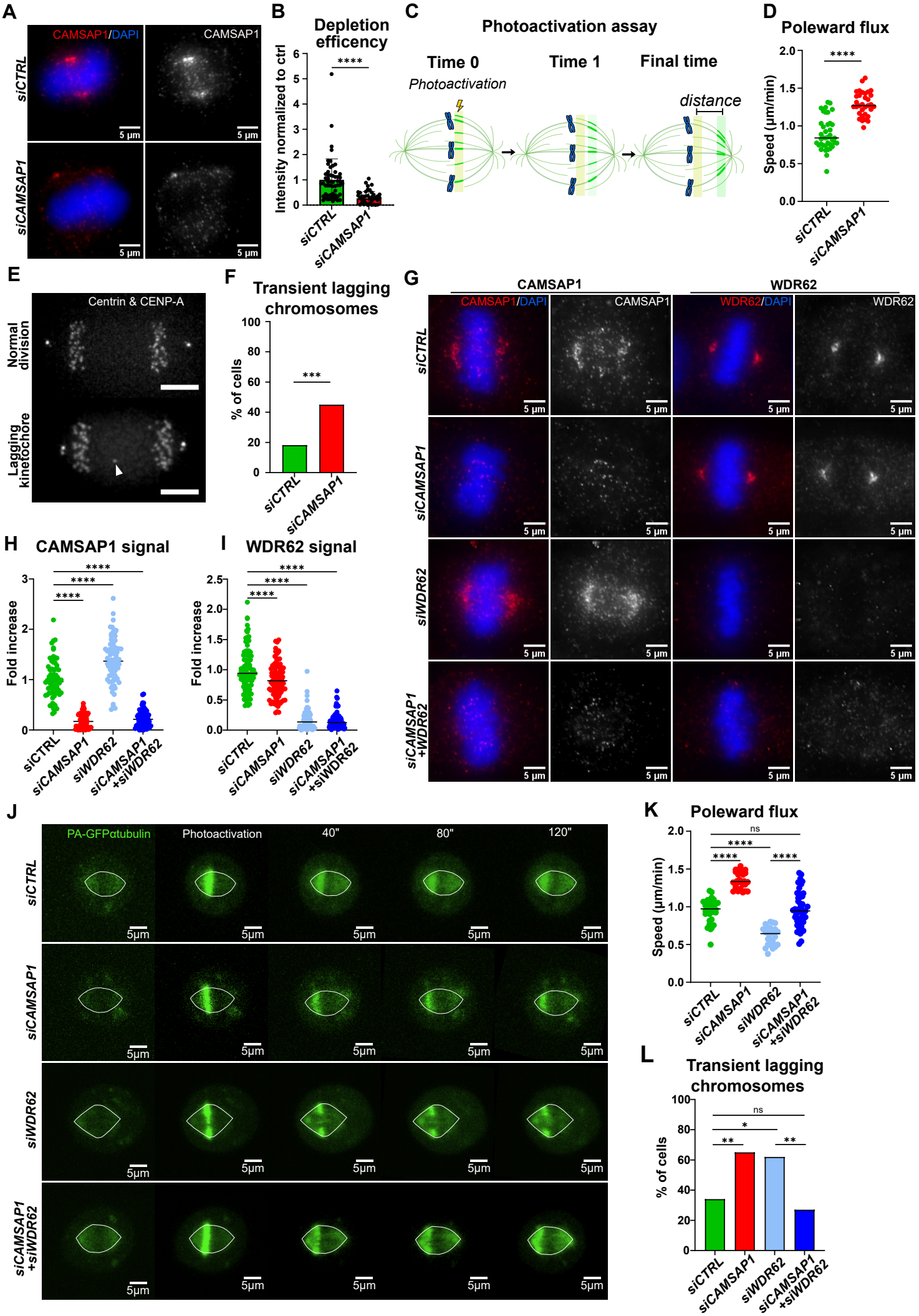

Figure 4 Doria, Ivanova et al.,

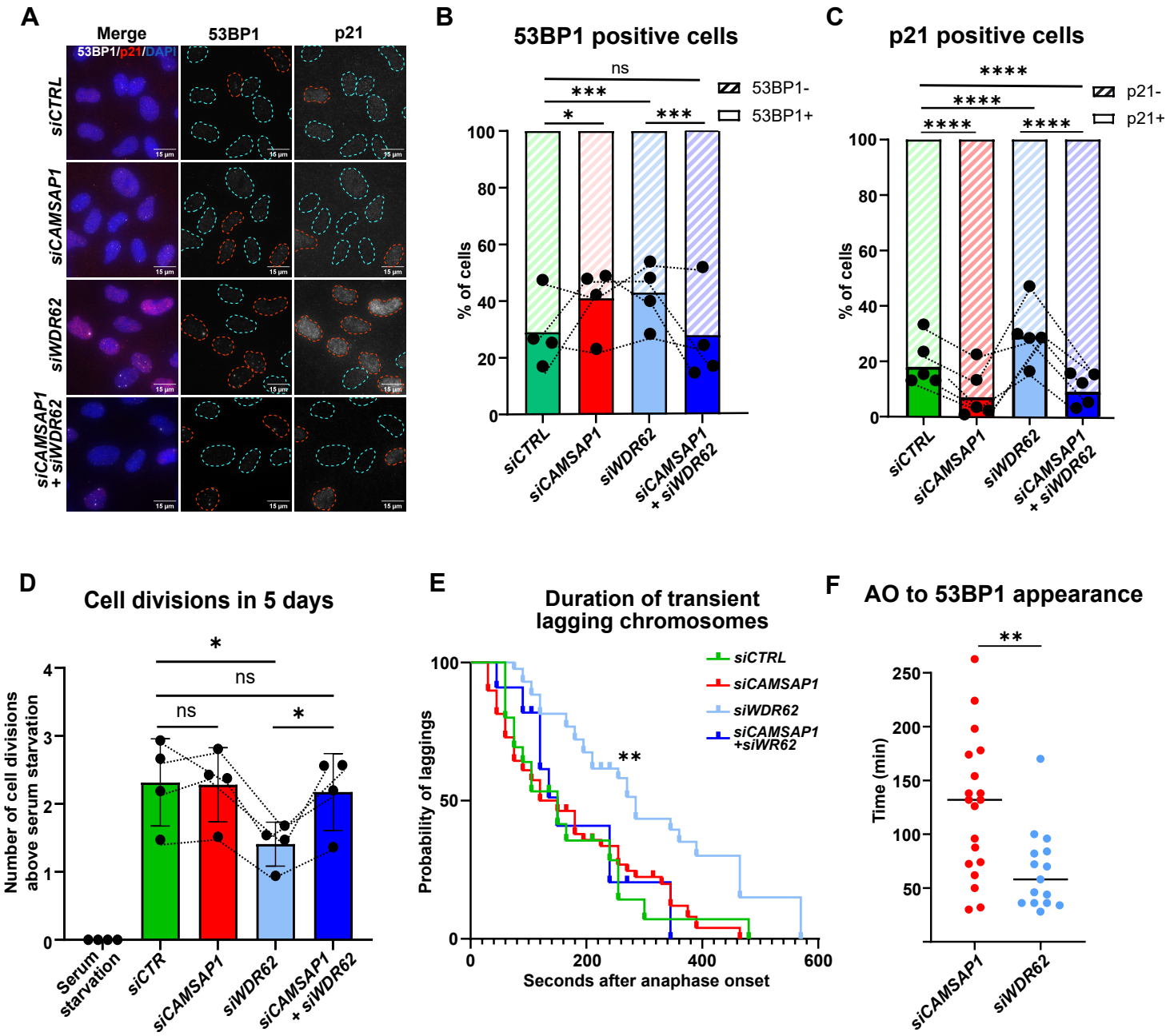

Figure 5 Doria, Ivanova et al.,

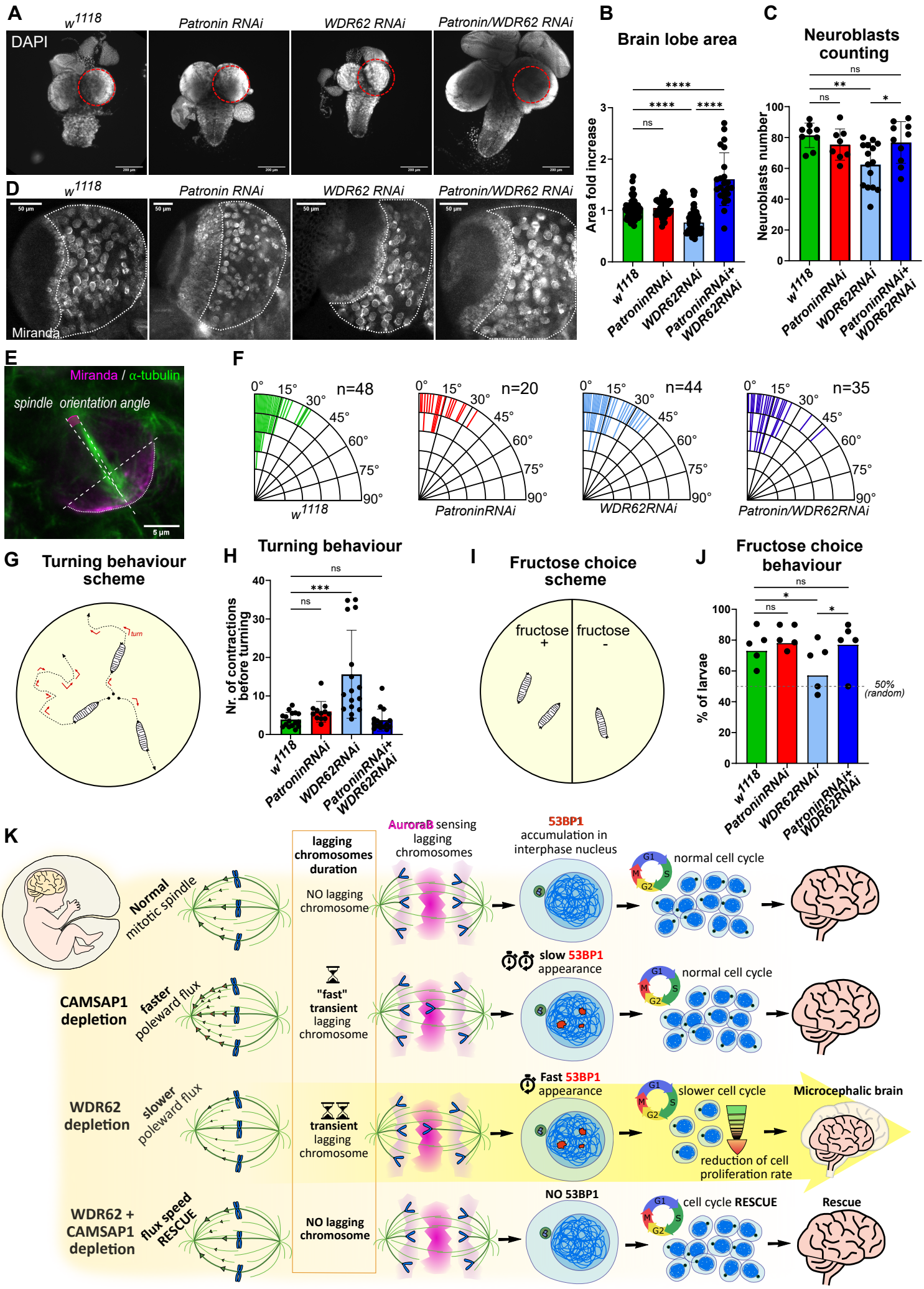

Supplementary Figure 1 Doria , Ivanova et al.,

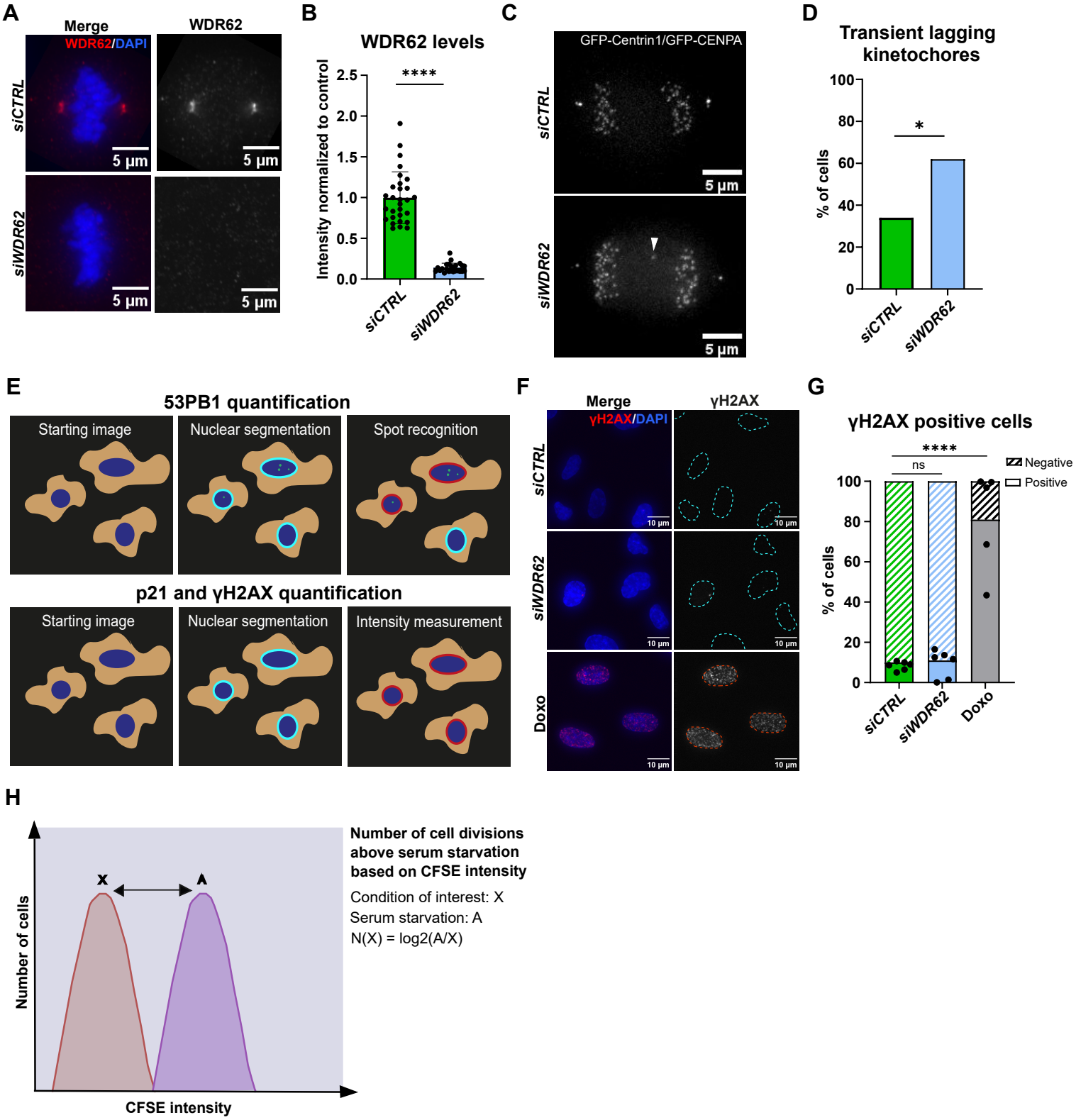

Supplementary figure 2 Doria, Ivanova et al.,

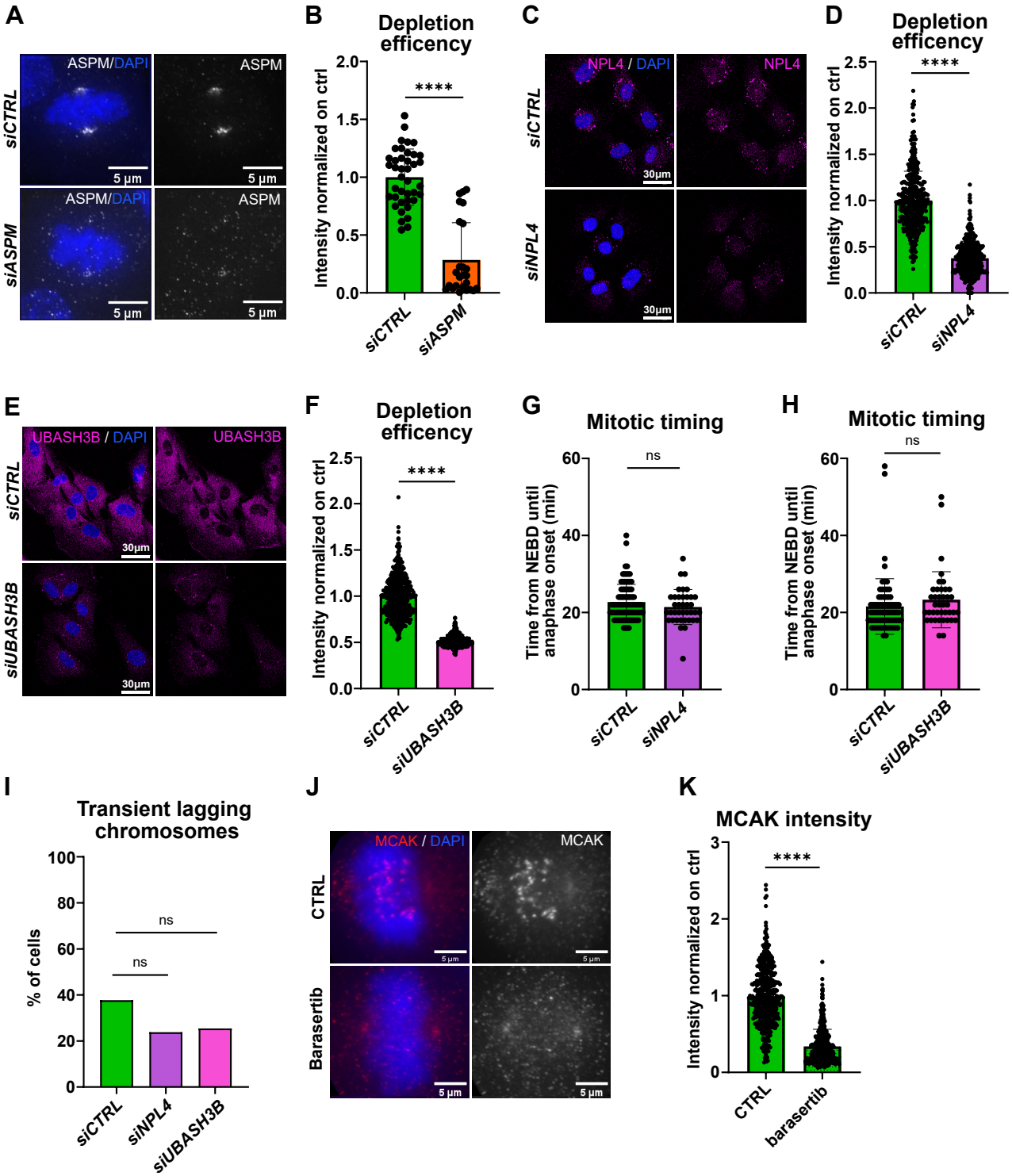

Supplementary Figure 3, Doria, Ivanova et al.,

A

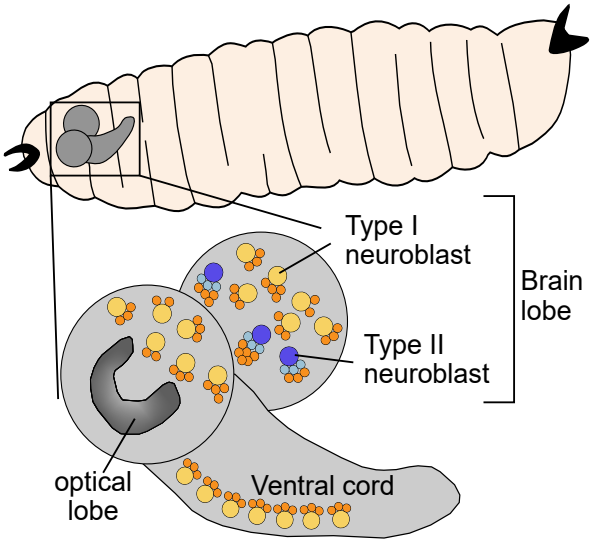

B

w^{1118}	♀ w^{1118} × ♂ $w;\frac{InscGAL4}{InscGAL4};\frac{+}{+}$ → $w;\frac{+}{InscGAL4};\frac{+}{+}$
Patronin	♀ $w;\frac{UAS\ Patronin\ RNAi}{UAS\ Patronin\ RNAi};\frac{+}{+}$ × ♂ $w;\frac{InscGAL4}{InscGAL4};\frac{+}{+}$ → $w;\frac{UAS\ Patronin\ RNAi}{InscGAL4};\frac{+}{+}$
WDR62	♀ $w;\frac{+}{+};\frac{UAS\ WDR62\ RNAi}{UAS\ WDR62\ RNAi}$ × ♂ $w;\frac{InscGAL4}{InscGAL4};\frac{+}{+}$ → $w;\frac{+}{InscGAL4};\frac{UAS\ WDR62\ RNAi}{+}$
Patronin +WDR62	♀ $w;\frac{UAS\ Patronin\ RNAi}{UAS\ Patronin\ RNAi};\frac{UAS\ WDR62\ RNAi}{UAS\ WDR62\ RNAi}$ × ♂ $w;\frac{InscGAL4}{InscGAL4};\frac{+}{+}$ → $w;\frac{UAS\ Patronin\ RNAi}{InscGAL4};\frac{UAS\ WDR62\ RNAi}{+}$

C

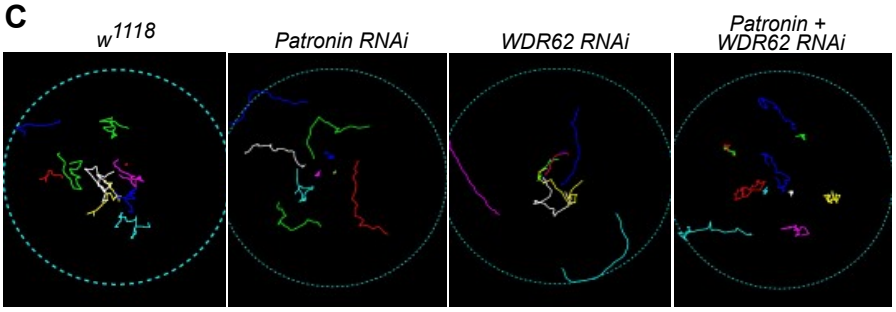
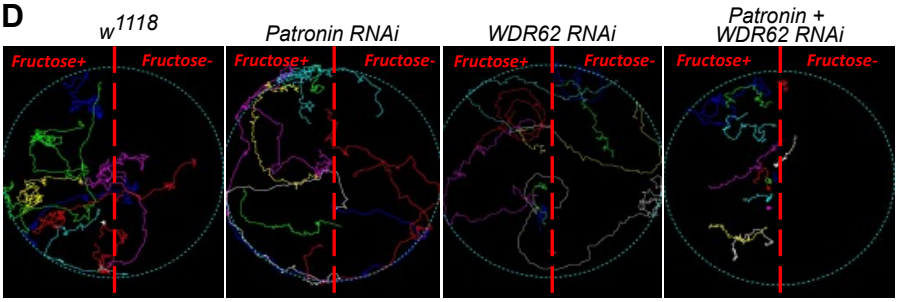
D